

# ClusIR: Towards Cluster-Guided All-in-One Image Restoration

Shengkai Hu<sup>1\*</sup> Jiaqi Ma<sup>2\*</sup> Jun Wan<sup>1†</sup>

Wenwen Min<sup>3</sup> Yongcheng Jing<sup>4</sup> Lefei Zhang<sup>5</sup> Dacheng Tao<sup>4</sup>

<sup>1</sup> Zhongnan University of Economics and Law, Wuhan, China

<sup>2</sup> Mohamed bin Zayed University of Artificial Intelligence, Abu Dhabi, UAE

<sup>3</sup> Yunnan University, Yunnan, China

<sup>4</sup> Nanyang Technological University, Singapore

<sup>5</sup> Wuhan University, Wuhan, China

shengkaihu@stu.zuel.edu.cn, jiaqi.ma@mbzuai.ac.ae, jun.wan@zuel.edu.cn

minwenwen@ynu.edu.cn, {yongcheng.jing, dacheng.tao}@ntu.edu.sg, zhanglefei@whu.edu.cn

## Abstract

*All-in-One Image Restoration (AiOIR) aims to recover high-quality images from diverse degradations within a unified framework. However, existing methods often fail to explicitly model degradation types and struggle to adapt their restoration behavior to complex or mixed degradations. To address these issues, we propose ClusIR, a Cluster-Guided Image Restoration framework that explicitly models degradation semantics through learnable clustering and propagates cluster-aware cues across spatial and frequency domains for adaptive restoration. Specifically, ClusIR comprises two key components: a Probabilistic Cluster-Guided Routing Mechanism (PCGRM) and a Degradation-Aware Frequency Modulation Module (DAFMM). The proposed PCGRM disentangles degradation recognition from expert activation, enabling discriminative degradation perception and stable expert routing. Meanwhile, DAFMM leverages the cluster-guided priors to perform adaptive frequency decomposition and targeted modulation, collaboratively refining structural and textural representations for higher restoration fidelity. The cluster-guided synergy seamlessly bridges semantic cues with frequency-domain modulation, empowering ClusIR to attain remarkable restoration results across a wide range of degradations. Extensive experiments on diverse benchmarks validate that ClusIR reaches competitive performance under several scenarios.*

## 1. Introduction

Image restoration aims to recover high-quality images from degraded observations such as noise, rain, haze, blur, and

\*Equal contribution.

†Corresponding author.

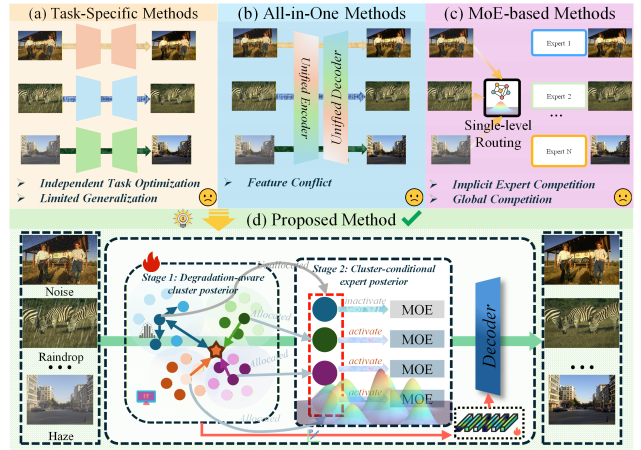


Figure 1. Comparison of common image restoration paradigms. (a) Task-specific methods train separate networks for each degradation. (b) All-in-one methods unify multiple degradations within a single encoder–decoder. (c) MoE-based methods introduce expert specialization via dynamic routing. (d) Our proposed ClusIR enables explicit degradation discrimination through a Probabilistic Cluster-Guided Routing Mechanism, resulting in improved robustness to complex and mixed degradations.

low light. As a fundamental task in low-level vision, it is vital for improving the performance of downstream applications, including detection [16, 46], tracking [18], and recognition [29]. Traditional approaches are typically task-specific, with each network tailored to a particular degradation type (Fig. 1(a)), such as denoising [5, 40, 65, 66, 69, 70], dehazing [2, 9, 12, 41], or low-light enhancement [3, 52–54, 63]. However, task-specific methods exhibit limited generalization capability, since models optimized for specific degradations often fail to adapt to unseen or complex degradation scenarios.

To address the limitations of task-specific models, re-

cent works have explored All-in-One Image Restoration (AiOIR), aiming to handle diverse degradations within a unified framework (Fig. 1(b)). Early methods like AirNet [22] introduced degradation encoders for feature extraction, while ProRes [31] and PromptIR [38] employed visual prompts for adaptive guidance. More recent approaches [4, 23, 26, 42] leverage large-scale vision models (e.g., CLIP [39], DINO [36]) to improve generalization. Despite their versatility, these unified frameworks often depend on shared representations, limiting degradation-specific adaptability and robustness under complex or hybrid conditions.

Recently, Mixture-of-Experts (MoE) frameworks [49, 56, 68, 71] (Fig. 1(c)) have enhanced AiOIR generalization by introducing expert specialization over shared representations. MEASNet [61] exploits pixel- and frequency-level cues to guide expert selection, while MoCE-IR [62] employs complexity-aware experts for dynamic resource allocation. MoFME [71] introduces an uncertainty-aware router to achieve scalable specialization, and UniRestorer [25] adopts multi-granularity degradation representations for unified restoration. However, they rely on implicit expert competition without explicit degradation separation, leading to overlapping activations and ambiguous routing.

Motivated by the above observations, we propose ClusIR (as shown in Fig. 1(d)), a **Cluster-Guided Image Restoration** framework that introduces clustering-based discrimination to decouple degraded semantics and stabilizes expert routing for adaptive image restoration. ClusIR consists of two key components: a Probabilistic Cluster-Guided Routing Mechanism (PCGRM) and a Degradation-Aware Frequency Modulation Module (DAFMM). PCGRM leverages hierarchically organized cluster prototypes to achieve discriminative and collaborative expert activation, thereby enabling explicit degradation separation and adaptive expert routing in the spatial domain. Meanwhile, DAFMM employs cluster-guided priors to enhance frequency self-mining and promote effective interaction between low- and high-frequency representations, facilitating unified structural and textural restoration under complex degradations.

Our main contributions are summarized as follows:

- (1) We propose ClusIR, an All-in-One image restoration framework which incorporates explicit degradation information to bridge spatial and frequency domains. It achieves state-of-the-art performance across multiple heterogeneous benchmarks, demonstrating strong generalization and robustness to diverse degradations.
- (2) We introduce PCGRM to leverage hierarchical degradation prototypes to disentangle degradation semantics from expert activation, thereby achieving discriminative routing and improved restoration adaptability.
- (3) We design DAFMM to leverage cluster-guided priors for adaptive frequency learning, enabling coordinated

enhancement of structural and textural components for robust image restoration under complex degradations.

## 2. Related Work

### 2.1. All-in-One image restoration

All-in-One image restoration aims to address multiple degradation types within a unified framework. Compared to task-specific [2, 3, 47, 52] and general image restoration [24, 64, 66], it offers superior model efficiency and greater practicality for real-world applications. Recent studies have advanced spatial modeling and receptive-field adaptivity in unified restoration. DSwinIR [51] introduces a Deformable Sliding Window Transformer with content-aware attention, while Cat-AIR [19] designs a content- and task-aware mechanism that balances local and global information through alternating spatial-channel attention. Beyond spatial modeling, another research line focuses on semantic adaptation through prompt learning. PromptIR [38] employs degradation-specific prompts for adaptive restoration, ProRes [31] encodes multiple degradation patterns into unified visual prompts for controllable restoration, and Zhang et al. [72] extend this idea via a two-stage quality-aware prompting scheme.

In parallel, frequency-domain approaches aim to jointly recover structural and textural details. CSNet [10] integrates channel-wise Fourier transforms with multi-scale frequency modules under a frequency-aware loss, FPro [73] combines frequency decomposition with prompt learning for joint structural-textural enhancement, and AdaIR [11] mines degradation-specific frequency priors via bidirectional frequency-spatial modulation. However, existing frequency-based frameworks still rely on implicit feature sharing across degradations, hindering explicit degradation modeling and generalization to unseen scenarios.

### 2.2. Mixture-of-Experts based image restoration

Mixture-of-Experts (MoE) mechanisms have recently been adopted in image restoration to enhance model capacity and task adaptivity via dynamic expert routing. Early work MEASNet [61] integrates frequency-domain priors into the MoE framework to jointly model spatial-frequency correlations for balanced structural-textural restoration. Yang et al. [56] exploit textual weather descriptions to construct language-driven degradation priors for expert selection, while WM-MoE [30] employs a weather-aware router and multi-scale experts for blind adverse-weather removal. MoCE-IR [62] utilizes complexity-aware experts with adaptive computational units for resource allocation based on degradation difficulty, and MoFME [71] designs feature-modulated experts with shared weights and an uncertainty-aware router for scalable specialization. UniRestorer [25] introduces multi-granularity degradation rep-

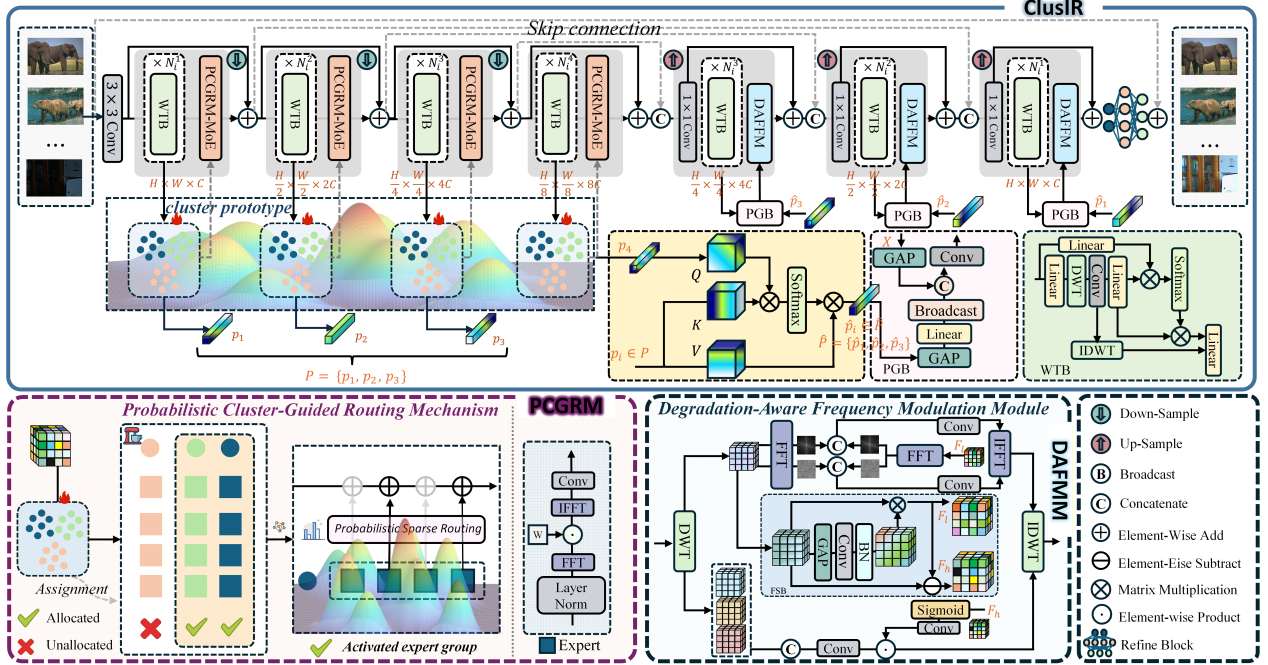


Figure 2. Overview of the proposed ClusIR framework, which integrates the Probabilistic Cluster-Guided Routing Mechanism (PCGRM) and the Degradation-Aware Frequency Modulation Module (DAFMM).

representations and a corresponding MoE model for unified restoration, while M2Restore [49] further advances this paradigm through a CLIP-guided MoE-based Mamba-CNN framework that unifies cross-modal priors with global-local modeling for adaptive, degradation-aware restoration.

While effective, existing paradigms exhibit inherent limitations. In contrast, our ClusIR explicitly organizes degradation representations via cluster prototypes, enabling discriminative expert activation and adaptive frequency enhancement within a unified architecture.

### 3. Methods

#### 3.1. Overall Pipeline

Given a degraded input image  $\mathbf{I} \in \mathbb{R}^{H \times W \times 3}$ , where  $H$  and  $W$  denote the spatial resolution, ClusIR first extracts shallow features using a  $3 \times 3$  convolution. These features are subsequently fed into a four-stage encoder, where each stage comprises a Wavelet-based Transformer Block (WTB) [59] and a Mixture-of-Experts (MoE) block driven by the proposed PCGRM. The PCGRM produces degradation-aware representations and hierarchical prompts (e.g.,  $p_1, p_2, p_3, p_4$ ). The multi-scale prompts  $p_1, p_2, p_3$  are then integrated with  $p_4$  via a multi-head cross-attention mechanism to generate semantic prompts  $\hat{p}_1, \hat{p}_2, \hat{p}_3$ . Each semantic prompt is refined by a lightweight Prompt Generation Block (PGB) [38] and injected into the DAFMM for frequency-domain modulation, enhancing the interaction between structural (low-frequency) and textural (high-

frequency) components. The decoder progressively reconstructs the restored image from the aggregated multi-scale features, ensuring consistent spatial-frequency recovery.

#### 3.2. Probabilistic Cluster-Guided Routing Mechanism

Current All-in-One MoE methods [25, 49, 61] predominantly adopt a single-stage routing paradigm, which directly predicts a flat expert distribution from the input features  $\mathbf{x}$ :

$$p(E = e | \mathbf{x}) = \text{Softmax}(\mathbf{w}^\top \mathbf{x}), \quad (1)$$

and aggregates expert outputs as:

$$\mathbf{y} = \sum_{e=1}^M p(E = e | \mathbf{x}) \cdot \mathcal{E}_e(\mathbf{x}). \quad (2)$$

where  $e$  is the expert index,  $M$  is the number of experts and  $\mathcal{E}_e(\mathbf{x})$  denotes the output of the  $e$ -th expert.  $\mathbf{y}$  denotes the restored image and  $\mathbf{w}$  is the parameter of the gating mechanism. The above routing design implicitly assumes a universal gating distribution (i.e., a **unimodal distribution**) across all degradations, ignoring their heterogeneous and compositional nature. This leads to two key issues: (1) Mixed degradations collapsed into a single distribution. Real-world degradations (e.g., noise + blur + haze) are inherently multi-modal, yet the single-stage softmax enforces a unimodal gating, causing semantic entanglement and limiting mixed-degradation modeling. (2) Unstable

global expert competition. Since the router must simultaneously infer degradations and select experts within the same probability space, experts compete globally, inducing gradient interference and training instability, which degrades degradation-aware representation learning and overall restoration quality.

To overcome these limitations, we propose a novel Probabilistic Cluster-Guided Routing Mechanism (PCGRM), which decomposes the routing into a **hierarchical two-stage process** that first infers a degradation-aware cluster posterior, followed by cluster-conditional expert routing, as detailed below:

$$\mathbf{y}(\mathbf{x}) = \sum_c p(C = c | \mathbf{x}) \sum_e p(E = e | c, \mathbf{x}) \mathcal{E}_e(\mathbf{x}), \quad (3)$$

where  $c$  denotes the index of the latent degradation type. This decomposition disentangles degradation perception and expert selection, yielding more stable and interpretable routing. Moreover, The proposed PCGRM models a **multimodal distribution**, making it possible to address image restoration under diverse and complex degradations.

**Stage 1: Degradation-aware cluster posterior**  $p(C = c | \mathbf{x})$ . To achieve explicit degradation discrimination and hierarchical representation modeling, we construct a hierarchy of cluster prototypes aligned with different encoder stages. Specifically, shallow encoders employ prototypes to capture diverse degradation patterns, while deeper encoders adopt prototypes to represent more compact and abstract degradation semantics.

For each encoder layer  $l$ , we construct a learnable prototype bank  $\mathbf{P}^{(l)} \in \mathbb{R}^{L \times D}$  to capture layer-specific degradation semantics. To enhance degradation discrimination and routing stability, we impose spherical normalization and near-orthogonality constraints on the prototype bank, ensuring that each prototype lies on a unit hypersphere with minimal pairwise correlation. For the encoded multi-scale features  $\mathbf{X} = \{\hat{\mathbf{x}}_i\}_{i=1}^B$ , where  $\hat{\mathbf{x}}_i \in \mathbb{R}^{H \times W \times D}$  and  $B$  is the batch size, global average pooling (GAP) is first applied to obtain compact feature representations, followed by a linear projection and normalization. Then, the cosine similarity between each normalized feature token  $\mathbf{x}_i$  and the cluster prototype  $\mathbf{P}_c^{(l)}$  at layer  $l$  is computed as:

$$\text{sim}(\mathbf{x}, C = c) = \frac{\mathbf{x}^\top \mathbf{P}_c}{\|\mathbf{x}\|_2 \|\mathbf{P}_c\|_2}. \quad (4)$$

For brevity, we omit the indices  $i$  and  $l$ . The degradation-aware cluster posterior is then obtained via a softmax normalization over all cluster prototypes:

$$\hat{\alpha}_c = \frac{\exp(\text{sim}(\mathbf{x}, C = c))}{\sum_{i=1}^N \exp(\text{sim}(\mathbf{x}, C = i))}, \quad (5)$$

where  $\hat{\alpha}_c$  denotes the probability that the token  $\mathbf{x}$  belongs to the  $c$ -th degradation cluster and  $N$  is the number of cluster

prototypes. With estimated probability, the topK method is used to choose the most probable cluster prototypes for degradation-aware routing:

$$p(C = c | \mathbf{x}) = \alpha_c = \frac{\exp(\text{sim}(\mathbf{x}, C = c))}{\sum_{i \in \{K_1\}} \exp(\text{sim}(\mathbf{x}, C = i))}, \quad (6)$$

where  $\{K_1\}$  denotes the set of selected cluster prototypes and  $\alpha_c$  denotes the probability of selecting the  $c$ -th cluster prototype.

**Stage 2: Cluster-conditional expert posterior**  $p(E = e | c, \mathbf{x})$ . After obtaining the degradation-aware cluster posterior from Stage 1, we activate experts within each selected cluster to enable degradation-aware routing. Assume that each cluster prototype carries a Gaussian semantic prior  $\mathcal{N}(\boldsymbol{\mu}_c, \text{diag}(\boldsymbol{\sigma}_c^2))$ , where  $\boldsymbol{\mu}_c \in \mathbb{R}^D$  and  $\text{diag}(\boldsymbol{\sigma}_c^2)$  represent the semantic center and feature uncertainty of the  $c$ -th cluster, respectively. We generate degradation prompts  $\mathcal{P}$  through reparameterization, weighted by the cluster posterior  $\alpha_c$ :

$$\mathcal{P} = \sum_{c=1}^N \alpha_c (\boldsymbol{\mu}_c + \boldsymbol{\sigma}_c \odot \boldsymbol{\epsilon}_c), \quad \text{s.t.} \quad \boldsymbol{\epsilon}_c \sim \mathcal{N}(\mathbf{0}, \mathbf{I}). \quad (7)$$

The injected Gaussian noise models intra-cluster uncertainty and continuous degradation variations, thereby mitigating prototype collapse and facilitating robust hierarchical routing under mixed and unseen degradations. Then, the prompt interacts with features through cross-attention to form a gating mechanism and the probability distribution over all experts within that cluster  $c$  can be computed as:

$$\mathbf{g} = \text{CrossAttn}(\mathbf{x}, \mathcal{P}, \mathcal{P}), \quad (8)$$

$$\pi_c = \text{Softmax}(\mathbf{W}_c \mathbf{g} + \mathbf{b}_c), \quad (9)$$

where  $\mathbf{W}_c$  is the learnable weight and  $\mathbf{b}_c$  serves as an interference term. Subsequently, the top  $K_2$  experts with the highest activation probabilities are selected to form the active expert subset. The probability that expert  $e$  is selected within cluster  $c$  can be formulated as follows:

$$p(E = e | c, \mathbf{x}) = \frac{\exp([\mathbf{W}_c \mathbf{g} + \mathbf{b}_c]_e)}{\sum_{e'=1}^{K_2} \exp([\mathbf{W}_c \mathbf{g} + \mathbf{b}_c]_{e'})}. \quad (10)$$

This two-stage probabilistic routing mechanism disentangles degradation recognition and expert activation, enabling the model to first discover potential degradation types and then specifically select experts in each cluster. By factorizing the decision space from a single flat expert distribution (i.e., a unimodal distribution) into a structured hierarchy (i.e., a multimodal distribution), the proposed PCGRM mitigates global expert interference and enables interpretable cluster-to-expert correspondence, thereby improving robustness to mixed and unseen degradations.

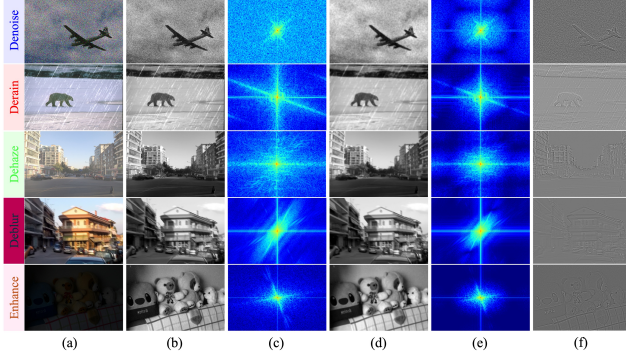


Figure 3. Motivation of the Frequency Self-Mining Block (FSB). (a): the input image; (b)&(c): the low-frequency subband and frequency spectrum via DWT; (d)&(e): the refined low-frequency response and frequency spectrum via the proposed DAFMM; (f): the high-frequency information further refined by the FSB based on (b). Our DAFMM effectively decompose low- and high-frequency information, thereby achieving better AiOIR performance.

### 3.3. Degradation-Aware Frequency Modulation Module

The proposed PCGRM explicitly decouples degradation perception and expert selection in the spatial domain, it primarily operates on global semantic representations. However, real-world degradations often exhibit frequency-dependent characteristics—for instance, high-frequency textures are more susceptible to noise, whereas low-frequency structural components are prone to blur. To bridge this gap, we extend the degradation modeling from the spatial to the frequency domain and introduce a Degradation-Aware Frequency Modulation Module (DAFMM) for fine-grained frequency enhancement. Specifically, by taking the cluster-aware semantic prompt  $\mathcal{P}$  as a degradation prior, DAFMM drives a dual-branch frequency processing pathway that adaptively restores low-frequency structures and refines high-frequency textures.

The DAFMM first decomposes the degradation-aware features into low- (i.e.,  $\hat{F}_{LL}$ ) and high-frequency components (i.e.,  $\{\hat{F}_{HL}, \hat{F}_{LH}, \hat{F}_{HH}\}$ ) through a discrete wavelet transform (DWT) as shown in Fig. 2. We visualize the low-frequency subband  $\hat{F}_{LL}$  in Fig. 3, and find that  $\hat{F}_{LL}$  still retains prominent edge structures (Fig. 3(b)) and residual mid-frequency components (Fig. 3(c)). The results reveal that the DWT cannot fully decouple structural and textural information, potentially leading to suboptimal performance in image restoration. To address this limitation, the proposed DAFMM incorporates a learnable Frequency Self-Mining Block (FSB) that adaptively disentangles global low-frequency structures from localized high-frequency details. Each frequency component is then refined through tailored modulation strategies, thereby achieving more effective image restoration.

**Frequency Self-Mining Block.** Given  $\hat{F}_{LL}$ , a learnable

low-pass filter is constructed by leveraging global average pooling (GAP) and generating softmax-normalized dynamic weights. Then, the  $\hat{F}_{LL}$  is unfolded into local patches and adaptively filtered to obtain the low-frequency component  $\mathcal{F}_l$ . The high-frequency component  $\mathcal{F}_h$  is obtained in a residual manner. The whole process can be formulated as:

$$W = \text{Softmax}(\text{BN}(\text{Conv}_{1 \times 1}(\text{GAP}(\hat{F}_{LL})))), \quad (11)$$

$$X = \text{Unfold}(\hat{F}_{LL}), \mathcal{F}_l = \sum_{i=1}^{k^2} W_i \odot X_i, \quad (12)$$

$$\mathcal{F}_h = \hat{F}_{LL} - \mathcal{F}_l, \quad (13)$$

where  $\odot$  is element-wise multiplication,  $i$  denotes index of each spatial element in the  $k^2$  patch. Hence, the FSB facilitates content-adaptive frequency decomposition by learning data-driven low-pass filtering, in contrast to conventional wavelet transforms that rely on fixed filter kernels, thereby achieving more accurate structural preservation and enhanced texture recovery.

**Low-Frequency Modulation.** As shown in Fig. 3(c), the obtained low-frequency representation still contains residual mid-frequency structures. To further refine its spectral purity, we perform amplitude-phase fusion in the Fourier domain, where structural cues (phase) and global intensity trends (amplitude) can be adaptively controlled, yielding cleaner and more expressive low-frequency features. The whole process can be formulated as follows:

$$\begin{aligned} \tilde{L} = \text{IFFT} \left( \mathcal{F}_{\text{conv1}} \left( \text{Concat}(\mathcal{A}_{\hat{F}_{LL}}, \mathcal{A}_{\mathcal{F}_l}) \right), \right. \\ \left. \mathcal{F}_{\text{conv2}} \left( \text{Concat}(\Phi_{\hat{F}_{LL}}, \Phi_{\mathcal{F}_l}) \right) \right), \end{aligned} \quad (14)$$

where  $\text{IFFT}(\cdot)$  denotes Inverse Fast Fourier Transform,  $\text{Concat}(\cdot)$  means channel concatenation, and  $\mathcal{A}(\cdot)$  and  $\Phi(\cdot)$  denote the amplitude and phase components, respectively.  $\mathcal{F}_{\text{conv1}}(\cdot)$  and  $\mathcal{F}_{\text{conv2}}(\cdot)$  represent adaptive fusion operations applied to the amplitude and phase in the spectral domain. This spectral redistribution transforms static DWT decomposition into a learnable low-frequency enhancement space, which promotes structure consistency and enables controllable contrast in image restoration.

**High-Frequency Modulation.** We also use the self-mined prior  $\mathcal{F}_h$  to further modulate the high-frequency subbands. Specifically, high-frequency subbands  $\hat{F}_{HL}, \hat{F}_{LH}, \hat{F}_{HH}$  are first concatenated and modulated by  $\mathcal{F}_h$  through channel-wise gating, and this process can be defined as follows:

$$\tilde{H} = \sigma(\mathbf{W}\mathcal{F}_h) \cdot [\hat{F}_{HL}, \hat{F}_{LH}, \hat{F}_{HH}], \quad (15)$$

where  $\mathbf{W}$  denotes a learnable projection. As shown in Fig. 3(f), this modulation adaptively emphasizes salient

Table 1. Results under three AiOIR tasks (**N+H+R**) setting with SOTA methods. The best and second-best results are highlighted in **bold** and underlined, respectively. Partial results are referenced from Perceive-IR [72].

Method	Venue	Denoising (CBSD68)			Dehazing	Deraining	Average
		$\sigma=15$	$\sigma=25$	$\sigma=50$	SOTS	Rain100L	
AirNet [22]	CVPR'22	33.92/0.932	31.26/0.888	28.00/0.797	27.94/0.962	34.90/0.967	31.20/0.910
IDR [67]	CVPR'23	33.89/0.931	31.32/0.884	28.04/0.798	29.87/0.970	36.03/0.971	31.83/0.911
ProRes [31]	arXiv'23	32.10/0.907	30.18/0.863	27.58/0.779	28.38/0.938	33.68/0.954	30.38/0.888
PromptIR [38]	NeurIPS'23	33.98/0.933	31.31/0.888	28.06/0.799	30.58/0.974	36.37/0.972	32.06/0.913
NDR [58]	TIP'24	34.01/0.932	31.36/0.887	28.10/0.798	28.64/0.962	35.42/0.969	31.51/0.910
Gridformer [48]	IJCV'24	33.93/0.931	31.37/0.887	28.11/0.801	30.37/0.970	37.15/0.972	32.19/0.912
InstructIR [8]	ECCV'24	<b>34.15/0.933</b>	31.52/0.890	28.30/0.804	30.22/0.959	37.98/0.978	32.43/0.913
Up-Restorer [28]	AAAI'25	33.99/0.933	31.33/0.888	28.07/0.799	30.68/0.977	36.74/0.978	32.16/0.915
Perceive-IR [72]	TIP'25	34.13/0.934	<b>31.53/0.890</b>	<b>28.31/0.804</b>	30.87/0.975	38.29/0.980	32.63/0.917
AdaIR [11]	ICLR'25	34.12/0.935	31.45/0.892	28.19/0.802	31.06/0.980	38.64/0.983	32.69/0.918
MoCE-IR [62]	CVPR'25	34.11/0.932	31.45/0.888	28.18/0.800	31.34/0.979	<b>38.57/0.984</b>	32.73/0.917
DFPIR [43]	CVPR'25	34.14/0.935	31.47/0.893	28.25/0.806	31.87/0.980	38.65/0.982	32.88/0.919
<b>ClusIR</b>	Ours	34.10/ <b>0.938</b>	31.45/ <b>0.897</b>	28.19/ <b>0.814</b>	<b>32.85/0.983</b>	<b>38.71/0.984</b>	<b>33.06/0.923</b>

Table 2. Results under five AiOIR tasks (**N+H+R+B+L**) setting with SOTA methods. Denoising reports only  $\sigma=25$  following [67].

Method	Venue	Denoising	Dehazing	Deraining	Deblurring	Low-light	Average
		CBSD68 ( $\sigma=25$ )	SOTS	Rain100L	GoPro	LOL	
TAPE [27]	ECCV'22	30.18/0.855	22.16/0.861	29.67/0.904	24.47/0.763	18.97/0.621	25.09/0.801
TransWeather [45]	CVPR'22	29.00/0.841	21.32/0.885	29.43/0.905	25.12/0.757	21.21/0.792	25.22/0.836
AirNet [22]	CVPR'22	30.91/0.882	21.04/0.884	32.98/0.951	24.35/0.781	18.18/0.735	25.49/0.846
IDR [67]	CVPR'23	<b>31.60/0.887</b>	25.24/0.943	35.63/0.965	27.87/0.846	21.34/0.826	28.34/0.893
PromptIR [38]	NeurIPS'23	31.47/0.886	26.54/0.949	36.37/0.970	28.71/0.881	22.68/0.832	29.15/0.904
Gridformer [48]	IJCV'24	31.45/0.885	26.79/0.951	36.61/0.971	29.22/0.884	22.59/0.831	29.33/0.904
InstructIR [28]	ECCV'24	31.40/0.887	27.10/0.956	36.84/0.973	29.40/0.886	23.00/0.836	29.55/0.907
Perceive-IR [72]	TIP'25	31.44/0.887	28.19/0.964	37.25/0.977	29.46/0.886	22.88/0.833	29.84/0.909
AdaIR [11]	ICLR'25	31.35/0.889	30.53/0.978	38.02/0.981	28.12/0.858	23.00/0.845	30.20/0.910
MoCE-IR [62]	CVPR'25	31.34/0.887	30.48/0.974	<b>38.04/0.982</b>	<b>30.05/0.899</b>	23.00/0.852	<b>30.58/0.919</b>
DFPIR [43]	CVPR'25	31.29/0.889	31.64/0.979	37.62/0.978	28.82/0.873	<b>23.82/0.843</b>	<b>30.64/0.913</b>
<b>ClusIR</b>	Ours	31.35/ <b>0.894</b>	<b>31.94/0.982</b>	37.28/0.980	28.54/0.872	<b>23.78/0.865</b>	<b>30.58/0.919</b>

edges and textures, enabling the model to capture fine-grained high-frequency structures with enhanced spectral fidelity. Finally, the enhanced low- and high-frequency features are progressively combined through inverse wavelet reconstruction, yielding the restored representation. Therefore, by incorporating semantic prompts with FSB, DAFMM effectively enhances both structural integrity and fine-grained texture details, thereby achieving more effective image restoration.

## 4. Experiments

### 4.1. Experimental Setup

**Datasets.** Following [22, 38, 72], we use three common training paradigms: *One-by-One* (single-task training), *All-in-One* (multi-task joint training), and *multi-degradation combination training*. For image denoising task, we combine the BSD400 [1] and WED [32] datasets, adding Gaussian noise with levels  $\sigma \in \{15, 25, 50\}$ , and evaluate on CBSD68 [33] and Kodak24 [13]. The dehazing task uses the RESIDE- $\beta$  [21] dataset, while deraining adopts Rain100L [57]. For deblurring and low-light enhancement, we employ the GoPro [34] and LOL [50] datasets, respectively. To develop a unified restoration model, we merge these datasets in a three (**N+H+R**) or five (**N+H+R+B+L**) degradation setting. For *multi-degradation combination training*, we use the CDD11 dataset [15], where multiple degradation types are jointly applied to a single image to simulate more realistic and challenging scenarios, and the

corresponding results are attached in supplementary material.

**Implementation Details.** For ClusIR, we employ the Adam optimizer ( $\beta_1=0.9$ ,  $\beta_2=0.999$ ) with an initial learning rate of  $2 \times 10^{-4}$  and a joint objective combining  $\ell_1$  and MS-SSIM losses [35]. The model is trained for 150 epochs with a batch size of 48, and the learning rate is halved after 75 epochs. Following [11], we set the data expansion ratios to 3, 120, 5, and 200 for denoising, deraining, deblurring, and low-light enhancement, respectively, while keeping dehazing unchanged. We set the cluster prototypes and activated clusters to [3, 3, 3, 3] and [2, 2, 2, 2], respectively, across all stages. Training is conducted on 4 NVIDIA A100 GPUs using random cropping and flipping with  $128 \times 128$  patches for data augmentation.

### 4.2. All-in-One Restoration Results

We evaluate ClusIR under two *All-in-One* configurations with progressively increasing complexity: a moderate three-degradation setting (**N+H+R**), a comprehensive five-degradation setting (**N+H+R+B+L**), and a composited degradation setting that involves multiple co-occurring degradations within a single image.

**Results Comparisons on Three Tasks:** Tab. 1 presents the quantitative comparison under the All-in-One (“**N+H+R**”) setting. ClusIR achieves the best overall performance with an average PSNR of 33.06 dB and SSIM of 0.923, surpassing all recent All-in-One methods. Compared with AdaIR, MoCE-IR, and DFPIR, ClusIR yields gains of +0.37

Table 3. Single-task restoration results, including denoising on Kodak24, dehazing on SOTS, deraining on Rain100L, deblurring on GoPro, and low-light enhancement on LOL. **Bold** and underline denote the best and the second best of AiOIR methods.

Kodak24	PSNR			SOTS	PSNR/SSIM	Rain100L	PSNR/SSIM	GoPro	PSNR/SSIM	LOL	PSNR/SSIM
	$\sigma = 15$	$\sigma = 25$	$\sigma = 50$								
DnCNN [69]	34.60	32.14	28.95	DehazeNet [2]	22.46/0.851	UMR [60]	32.39/0.921	DeblurGAN [20]	28.70/0.858	URetinex [52]	21.33/0.835
FFDNet [70]	34.63	32.13	28.98	FDGAN [12]	23.15/0.921	LPNet [14]	33.61/0.958	Stripformer [44]	33.08/0.962	SMG [55]	23.81/0.809
ADFNNet [40]	34.77	32.22	29.06	DehazeFormer [41]	31.78/0.977	DRSformer [6]	38.14/0.983	HI-Diff [7]	33.33/0.964	Retinexformer [3]	25.16/0.845
MIRNet-v2 [66]	34.29	31.81	28.55	Restormer [65]	30.87/0.969	Restormer [65]	36.74/0.978	MPRNet [64]	32.66/0.959	MIRNet [63]	24.14/0.835
Restormer [65]	34.78	32.37	29.08	NAFNet [5]	30.98/0.970	NAFNet [5]	36.63/0.977	Restormer [65]	32.92/0.961	Restormer [65]	22.43/0.823
NAFNet [5]	34.27	31.80	28.62	FSNet [9]	31.11/0.971	FSNet [9]	37.27/0.980	FSNet [9]	33.29/0.963	DiffIR [53]	23.15/0.828
AirNet [22]	34.81	32.44	29.10	AirNet [22]	23.18/0.900	AirNet [22]	34.90/0.977	AirNet [22]	31.64/0.945	AirNet [22]	21.52/0.832
IDR [67]	34.78	32.42	29.13	PromptIR [38]	31.31/0.973	PromptIR [38]	37.04/0.979	PromptIR [38]	<u>32.41/0.956</u>	PromptIR [38]	22.97/0.834
Perceive-IR [72]	34.84	<b>32.50</b>	29.16	Perceive-IR [72]	<u>31.65/0.977</u>	Perceive-IR [72]	<b>38.41/0.984</b>	Perceive-IR [72]	<b>32.83/0.960</b>	Perceive-IR [72]	<u>23.79/0.841</u>
<b>ClusIR (Ours)</b>	<b>35.06</b>	<b>32.60</b>	<b>29.49</b>	<b>ClusIR (Ours)</b>	<b>32.67/0.983</b>	<b>ClusIR (Ours)</b>	<b>37.52/0.980</b>	<b>ClusIR (Ours)</b>	30.07/0.904	<b>ClusIR (Ours)</b>	<b>23.82/0.852</b>

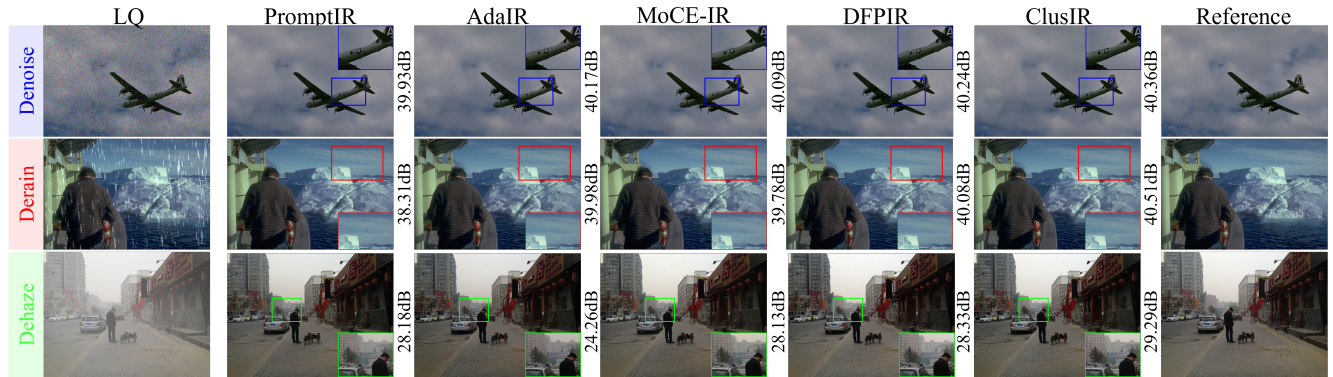


Figure 4. Visual comparison of ClusIR with SOTA AiOIR methods under the “N+H+R” setting. More visualization results are provided in the supplementary materials.

dB/+0.005, +0.33 dB/+0.006, and +0.18 dB/+0.004 in average PSNR/SSIM, respectively. Notably, ClusIR achieves new state-of-the-art results on dehazing (32.85/0.983) and deraining (38.71/0.984), while maintaining competitive denoising accuracy across all noise levels. These improvements demonstrate that the proposed PCGRM and DAFMM jointly enhance cross-degradation generalization and structural fidelity in complex restoration scenarios.

**Results Comparisons on Five Tasks:** Tab. 2 summarizes the results under this more challenging five-degradation setting. ClusIR achieves the second-highest PSNR (30.58 dB) and the best SSIM (0.919) among all competing All-in-One methods. Notably, ClusIR delivers leading performance in dehazing, outperforming AdaIR, MoCE-IR, and DFPIR with a score of 31.94/0.982, and also achieves clear gains in low-light enhancement, attaining +0.015 and +0.024 SSIM over AdaIR and DFPIR, respectively. For denoising, deraining, and deblurring, ClusIR maintains competitive performance, reaching 31.35/0.894, 37.28/0.980, and 28.54/0.872, respectively, which demonstrates its stable restoration capability across the remaining tasks.

### 4.3. Visual Results

As shown in Fig. 4, ClusIR consistently improves texture fidelity and structural coherence across diverse degradations. In the red, blue, and green regions, it restores finer details,

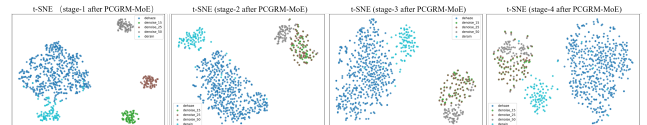


Figure 5. t-SNE visualization of cross-stage feature distributions after the PCGRM-MoE under the “N+H+R” setting.

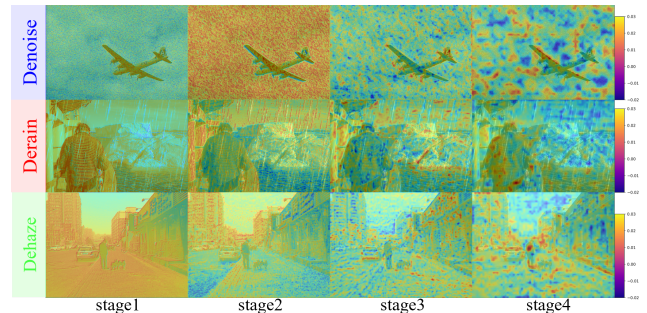


Figure 6. Visual degradation of PCGRM-MoE under the “N+H+R” setting. Higher values mean stronger correlations.

removes rain streaks more thoroughly, and reconstructs depth-consistent structures with balanced contrast, outperforming PromptIR, AirNet, and MoCE-IR. This improvement can be attributed to the strong degradation discrimination and semantic perception provided by the PCGRM. The t-SNE visualizations in Fig. 5 further depict a coherent representational evolution, where diverse degradation fea-

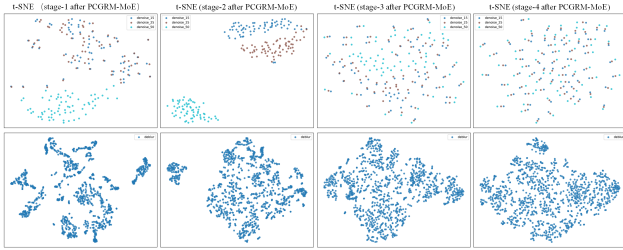


Figure 7. t-SNE visualization of cross-stage feature distributions after the PCGRM-MoE under the One-by-One setting.

tures that are initially well separated progressively converge within related degradation families (e.g., denoise-15/25/50), while maintaining clear distinctions across different tasks (e.g., denoising, deraining, and dehazing). This reveals a degradation-level discrimination to semantic alignment by cluster prototypes.

Moreover, the stage-wise prototype affinity maps in Fig. 6 reveal a progressive shift from localized degradation activations to globally coherent semantic responses. In the early stages (e.g., stage 1 and stage 2), the activations are concentrated on task-specific degraded regions, reflecting explicit degradation-type discrimination. In contrast, deeper stages exhibit more diffuse and semantically structured responses, capturing abstract regularities of scene content. Collectively, these analyses confirm that ClusIR effectively bridges degradation-specific cues and global structural semantics through hierarchical, degradation-aware representations.

#### 4.4. One-by-One Restoration Results

We evaluate ClusIR under the *One-by-One* setting (Tab. 3), where each restoration task is trained and tested independently. Top lines are task-specific and general methods, and the bottom lines refer to AiOIR methods.

As shown in Tab. 3, ClusIR achieves the best denoising performance on Kodak24, consistently ranking first in all noise levels. Notably, it reaches 35.06 dB at  $\sigma = 15$ , surpassing Perceive-IR and Restormer by +0.22 dB and +0.28 dB, respectively. On the dehazing task, ClusIR leads on SOTS, attaining 32.67/0.983 on SOTS, outperforming DehazeFormer and Perceive-IR. For deraining, it achieves 37.52/0.980 on Rain100L. On the low-light enhancement task, ClusIR yields 23.82/0.852, ranking first in AiOIR methods. For deblurring, HI-Diff and FSNet lead the performance due to their dedicated blur-handling designs.

Building on these results, we further examine the feature distributions in the single-task scenario. As illustrated in Fig. 7, ClusIR fails to effectively activate the cluster prototypes, which undermines the PCGRM, prevents reliable degradation discrimination, and consequently limits the generation of semantic prompts. In contrast, for the denoising task, ClusIR treats different Gaussian noise levels as distinct degradation types during joint training, allow-

Table 4. Ablation study on the impact of key components. Each module contributes complementary gains.

Index	WTB	PCGRM-MoE	DAFMM	avg PSNR $\uparrow$	avg SSIM $\uparrow$
(a)	✓			32.68	0.922
(b)	✓	✓		32.95	0.922
(c)	✓	✓	✓	33.06	0.923

ing cluster semantics to emerge progressively across stages. Specifically, at stage 1, the separability among noise levels remains ambiguous; by stage 2, noticeable degradation discrimination begins to appear; and by stage 4, the features of the same sample across  $\sigma=15/25/50$  become closer to each other after being refined by the PCGRM-MoE, while the features of different samples become more widely separated. These visual results further demonstrate the effectiveness of ClusIR in handling diverse degradation types.

#### 4.5. Ablation Study

We conduct the ablation studies to demonstrate the effectiveness of our proposed ClusIR. The results are reported under the “‘N+H+R” setting. Due to the page limitation, more detailed results are attached in the supplementary materials.

**Impact of Key Components.** We progressively integrate the MoE-PCGRM and the DAFMM into the baseline. As shown in Tab. 4, the performance improves progressively from (a) to (c). Using only the WTB in (a) provides basic restoration ability, yielding an average PSNR/SSIM of 32.68/0.922. Introducing PCGRM-MoE in (b) yields clear gains of +0.27 dB. Further incorporating DAFMM in (c) raises the average PSNR/SSIM to 33.06/0.923. These results can be attributed to PCGRM, which explicitly encodes degradation semantics and encourages more specialized expert behavior. Moreover, DAFMM further enhances both high- and low-frequency information through frequency self-mining.

**Impact of Cluster Prototype Numbers across Stages.** To investigate the influence of the cluster configuration on the hierarchical representation, we vary the number of prototype clusters across stages. As shown in Tab. 5, a uniform cluster prototype configuration (1) achieves the best balance between discrimination and consistency (33.06/0.923), while the unbalanced design (2) and (3) both lead to performance degradation. This decline indicates the improper allocation of cluster prototypes: excessive prototypes in shallow stages cause over-segmentation of degradation cues and interfere with low-level features learning, whereas excessive prototypes in deeper stages result in semantic dispersion and inconsistency among degradation types.

Table 5. Ablation on the impact of cluster prototypes across stages. We vary the number of cluster prototypes in each stage.

Index	Cluster prototype numbers (stage1–4)	avg PSNR	avg SSIM
(1)	[3, 3, 3, 3]	33.06	0.923
(2)	[2, 3, 4, 6]	32.27	0.912
(3)	[6, 4, 3, 2]	32.40	0.912

## 5. Conclusion

In this paper, we present ClusIR, an All-in-One image restoration framework that leverages explicit degradation cues to unify spatial and frequency-domain information processing. The explicit degradation cues are learned via the proposed PCGRM, which incorporates a hierarchical two-stage process that first infers a degradation-aware cluster posterior and then performs cluster-conditional expert routing. Building on this, DAFMM utilizes cluster-guided priors for adaptive frequency modulation, enabling coordinated enhancement of structural and textural components. Extensive experiments on diverse benchmarks demonstrate that ClusIR delivers competitive performance across AiOIR tasks, validating the effectiveness of our cluster-guided spatial–frequency modeling paradigm.

# ClusIR: Towards Cluster-Guided All-in-One Image Restoration

## Supplementary Material

### 6. Experimental Settings

#### 6.1. Datasets

**One-by-One Degradations setting.** For the single task image restoration, we follow the standard evaluation protocols and construct three independent restoration tasks: denoising, deraining, and dehazing. For image denoising, we combine the BSD400 [1] and WED [32] datasets as the training set, where BSD400 contains 400 images and WED provides 4,744 images. The images are corrupted with Gaussian noise at levels  $\sigma \in \{15, 25, 50\}$ . The denoising performance is evaluated on CBS68 [33] and Urban100 [17]. For deraining, we adopt the Rain100L [57] dataset, which includes 200 image pairs for training and 100 pairs for testing. For dehazing, we use the SOTS [21] dataset, consisting of 72,135 training images and 500 testing images. Each task is trained individually under this setting.

**Three Degradations Setting.** For the All-in-One “N+H+R” configuration, we integrate the three degradation tasks—denoising, deraining, and dehazing—into a unified model. The training set is constructed by merging the BSD400+WED (denoising), Rain100L (deraining), and SOTS (dehazing) datasets. The model is trained for 150 epochs on this combined dataset and evaluated on the corresponding test sets for each restoration task.

**Five Degradations setting.** The Five-Degradation “N+H+R+B+L” setting builds upon the Three-Degradation setting, adding two additional tasks: deblurring and low-light enhancement. For deblurring, we adopt the GoPro dataset [34], which consists of 2,103 training images and 1,111 testing images. For low-light enhancement, we use the LOL-v1 dataset [50], containing 485 training images and 15 testing images. It is important to note that for the denoising task under the Five-Degradation setting, we report results using Gaussian noise with  $\sigma = 25$ . The training takes 150 epochs.

**Composited Degradation setting.** For the composite degradation setting, we adopt the CDD11 [15] dataset. CDD11 contains 1,183 training images, including: (i) four single-degradation types: haze (H), low-light (L), rain (R), and snow (S); (ii) five double-degradation types: low-light + haze (L+H), low-light + rain (L+R), low-light + snow (L+S), haze + rain (H+R), and haze + snow (H+S); (iii) two triple-degradation types: low-light + haze + rain (L+H+R) and low-light + haze + snow (L+H+S). We train the model for 200 epochs while keeping all other settings unchanged.

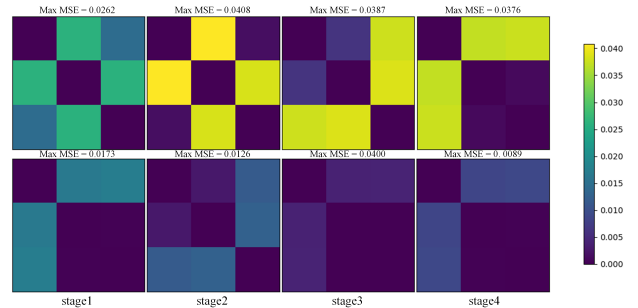


Figure 8. Pairwise prototype MSE across stages under orthogonal (top) and random (bottom) initialization. Orthogonal initialization yields consistently larger inter-prototype distances, indicating better degradations separability.

### 7. All-in-One Restoration Result

We extend the previous AiOIR settings by constructing various composite degradation scenarios, resulting in eleven distinct restoration settings in total.

**Results Comparisons on Composited Degradations:** Tab. 6 presents a comparison of ClusIR with state-of-the-art methods on the CDD11 dataset under Composited Degradation setting. ClusIR outperforms existing methods in terms of both PSNR and SSIM across all degradation combinations. Specifically, ClusIR achieves the highest performance, with an average PSNR of 27.33 dB and SSIM of 0.878, surpassing AirNet [22], PromptIR [38], WGWS-Net [74], and WeatherDiff [37] by gains of +3.58 dB / +0.075, +1.43 dB / +0.028, +0.37 dB / +0.015, and +4.84 dB / +0.079, respectively. Notably, for the CDD11-Double and CDD11-Triple settings, ClusIR consistently delivers superior performance, highlighting its robustness in handling multiple types of image degradation. Overall, these results demonstrate ClusIR’s effectiveness in all-in-one image restoration, showcasing its ability to simultaneously address multiple degradation tasks with a single unified model. These improvements can be attributed to our proposed PCGRM, which not only enables effective degradation discrimination but also activates the corresponding expert groups, facilitating the integration of specialized knowledge to handle diverse degradation types efficiently.

### 8. Ablation Studies

We conduct several ablation experiments to demonstrate the effectiveness of our proposed ClusIR. We report the results under the Three Degradations Setting.

**Model Scaling.** We propose two variants of ClusIR

Table 6. Comparison to state-of-the-art on composited degradations. PSNR (dB) and SSIM are reported on full RGB images.

Method	Params.	CDD11-Single				CDD11-Double					CDD11-Triple		Avg.
		L	H	R	S	L+H	L+R	L+S	H+R	H+S	L+H+R	L+H+S	
AirNet [22]	9M	24.83/.778	24.21/.951	26.55/.891	26.79/.919	23.23/.779	22.82/.710	23.29/.723	22.21/.868	23.29/.901	21.80/.708	22.24/.725	23.75/.814
PromptIR [38]	36M	26.32/.805	26.10/.969	31.56/.946	31.53/.960	24.49/.789	25.05/.771	24.51/.761	24.54/.924	27.05/.925	23.74/.752	23.33/.747	25.90/.850
WGWSNet [74]	26M	24.39/.774	27.90/.982	33.15/.964	34.43/.973	24.27/.800	25.06/.772	24.60/.765	27.23/.955	27.65/.960	23.90/.772	23.97/.771	26.96/.863
WeatherDiff [37]	83M	23.58/.763	21.99/.904	24.85/.885	24.80/.888	21.83/.756	22.69/.730	22.12/.707	21.25/.868	21.99/.868	21.23/.716	21.04/.698	22.49/.799
<b>ClusIR (Ours)</b>	55M	<b>26.62/.825</b>	<b>28.58/.982</b>	<b>32.59/.964</b>	<b>33.52/.9749</b>	<b>24.87/.8144</b>	<b>25.60/.7989</b>	<b>25.41/.795</b>	<b>27.52/.955</b>	<b>27.48/.960</b>	<b>24.31/.780</b>	<b>24.18/.782</b>	<b>27.33/.878</b>

with different scales, namely Small (ClusIR-S) and Tiny (ClusIR-T), as shown in Tab. 7.

**Efficiency Comparison.** As illustrated in Tab. 8, ClusIR-T achieves a significant reduction in computational cost compared to the base model, with only 6.89M parameters and 3.79G FLOPs. Despite this, it maintains competitive performance, achieving 31.98dB/0.916. ClusIR-S strikes a balance between model size and computational efficiency with 25.03M parameters and 13.42G FLOPs. Notably, ClusIR-T surpasses AirNet [22] by +0.78dB/0.006 while ClusIR has fewer parameters.

Table 7. Details of our base, small, and tiny variants of ClusIR. FLOPs are computed on an input of size  $128 \times 128$  using a NVIDIA 3060 GPU.

Architecture	ClusIR-Base	ClusIR-S	ClusIR-T
The Input Embedding Dimension	48	32	16
Params.	54.66M	25.03M	6.89M
FLOPs	28.85G	13.42G	3.79G

Table 8. Performance of different ClusIR (T/S/Base) on three degradation tasks. PSNR and SSIM are reported on full RGB images.

Architecture	Denoise			Derain	Dehaze	Avg.
	$\sigma=15$	$\sigma=25$	$\sigma=50$			
ClusIR-T	33.70/0.933	31.06/0.890	27.77/0.806	35.44/0.970	31.92/0.981	31.98/0.916
ClusIR-S	34.07/0.937	31.41/0.896	29.11/0.813	37.38/0.980	33.06/0.981	32.21/0.921
ClusIR-Base	34.10/0.938	31.45/0.897	28.19/0.814	38.71/0.984	32.85/0.983	33.06/0.923

Table 9. Impact of Orthogonal Initialization on Model Performance.

Initialization	Denoise			Derain	Dehaze	Avg.
	$\sigma=15$	$\sigma=25$	$\sigma=50$			
Orthogonal	34.10/0.938	31.45/0.897	28.19/0.814	38.71/0.984	32.85/0.983	33.06/0.923
Random	34.12/0.937	31.45/0.897	28.17/0.813	38.28/0.983	32.16/0.982	32.84/0.922

**Orthogonal Initialization.** To evaluate the effect of orthogonal initialization, we replace it with uniformly random prototype initialization for comparison.

As shown in Tab. 9, orthogonal initialization consistently improves performance across all tasks, achieving an average PSNR/SSIM of 33.06/0.923 and clearly surpassing the randomly initialized counterpart. This advantage stems from the strengthened degradation discrimination induced by orthogonal cluster prototypes. As visualized in Fig. 8,

the maximum inter-cluster MSE under orthogonal initialization reaches 0.0262/0.0408 in Stage 1 and Stage 2, respectively, whereas the non-orthogonal counterpart yields only 0.0173/0.0126. The orthogonal initialization produces significantly larger inter-prototype distances, where degradation cues are most distinct. In deeper stages, the prototypes gradually exhibit the emergence of semantic structure while still preserving meaningful separation among degradation types, indicating that orthogonality provides a stable prior throughout the hierarchy. Overall, the proposed orthogonal initialization enhances prototype separability, reduces semantic overlap among clusters, and leads to more discriminative representations.

## 9. Visualization

We provide more visual comparisons for the One-by-One Degradations setting, Three Degradations setting and a more complex Five Degradations settings.

### 9.1. Visual Comparison under One Degradations

As shown in Fig. 10, 11, 12, 13 and 14, we compare our ClusIR against recent state-of-the-art methods, including AirNet [22] (CVPR’22) and AdaIR [11] (ICLR’25).

Across all single degradation, ClusIR produces cleaner structures, sharper textures, and fewer residual artifacts, demonstrating that its cluster-guided modeling remains highly effective even when the degradation type is fixed.

### 9.2. Visual Comparison under Three Degradations

As shown in Fig. 15, 16, 17, 18, and 19, we compare our ClusIR against recent state-of-the-art methods, including AdaIR [11] (ICLR’25), DFPIR [43] (CVPR’25), and MoCE-IR [62] (CVPR’25).

Across all degradation types, ClusIR consistently preserves higher fidelity while maintaining fine textures and structural details. The zoomed-in regions further highlight ClusIR’s superiority in recovering sharp edges and realistic patterns compared to other approaches. These visual results are consistent with the quantitative improvements reported earlier.

### 9.3. Visual Comparison under Five Degradations

As some methods do not provide visual results under the five-degradation setting (N+H+R+B+L), we select Instruc-

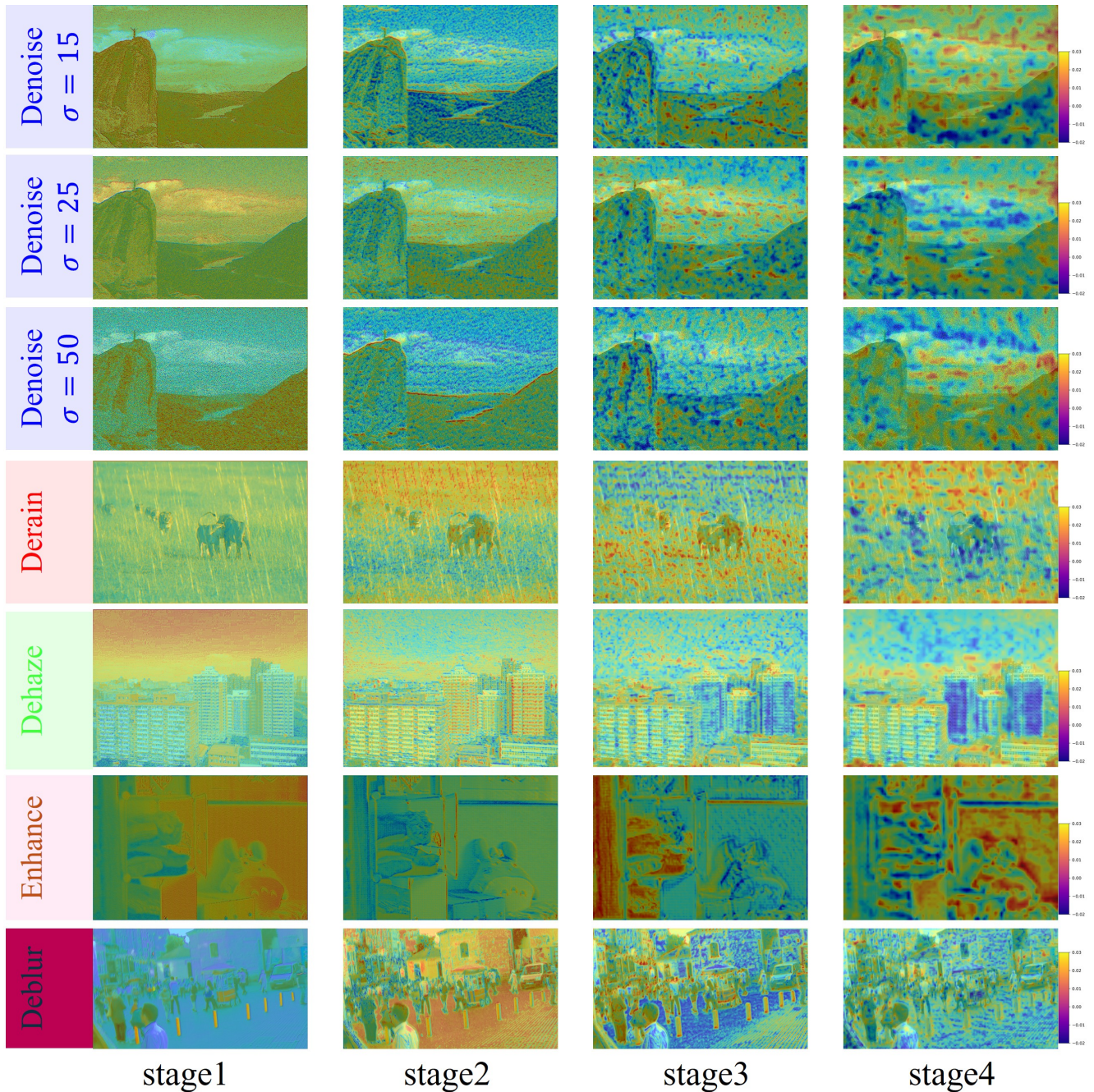


Figure 9. Visual degradation of PCGRM-MoE under the (N+H+R+B+L) setting. Higher values mean stronger correlations.

tIR [8] (ECCV’24) and MoCE-IR [62] (CVPR’25) for comparison with our ClusIR.

Zoom-in views in Fig. 20, 21, 22, 23, and 24 reveal that ClusIR better preserves both textural and structural details, producing results that are visually closer to the reference images. These observations indicate better restoration quality compared to the competing methods. Further, we visualized the features after PCGRM-MoE under the com-

plex scenario of the five-task degradation setting (Fig. 9). PCGRM achieved clear degradation feature discrimination in the shallow stages (i.e., stage 1-2), and gradually transitioned from degradation discrimination to semantic feature fusion in stages 3-4. This demonstrates the effectiveness of the PCGRM in progressively refining and integrating degradation-specific features into semantic representations across multiple stages.

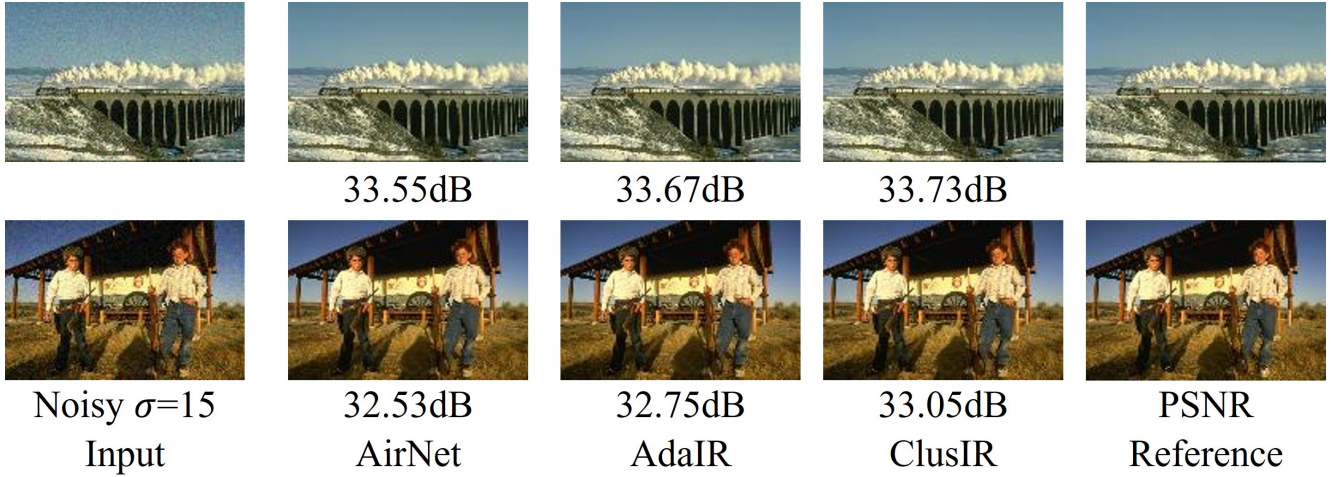


Figure 10. Denoising ( $\sigma = 15$ ) visual comparisons of ClusIR with state-of-the-art All-in-One methods under One-by-One setting.



Figure 11. Denoising ( $\sigma = 25$ ) visual comparisons of ClusIR with state-of-the-art All-in-One methods under One-by-One setting.



Figure 12. Denoising ( $\sigma = 50$ ) visual comparisons of ClusIR with state-of-the-art All-in-One methods under One-by-One setting.

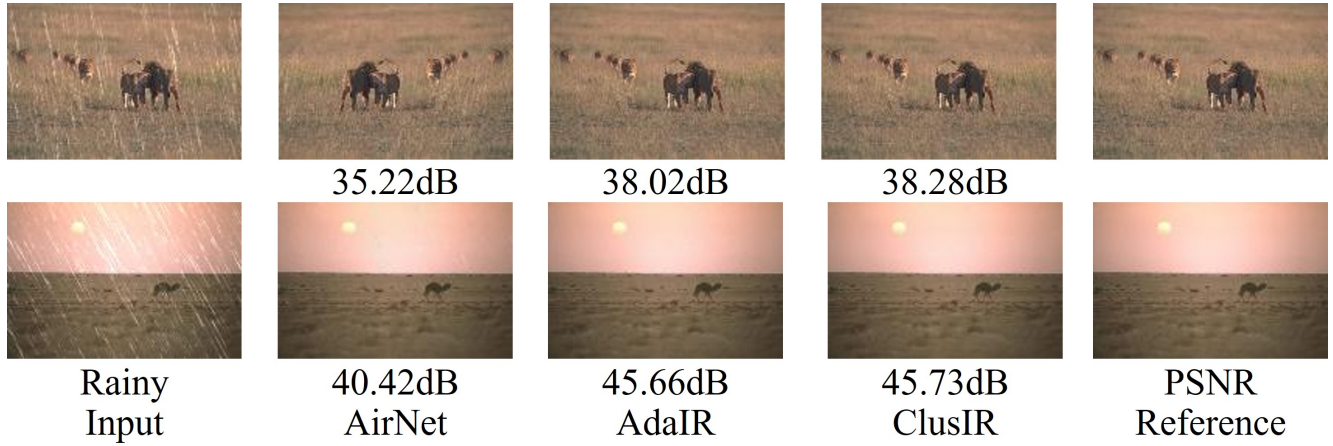


Figure 13. Deraining visual comparisons of ClusIR with state-of-the-art All-in-One methods under One-by-One setting.

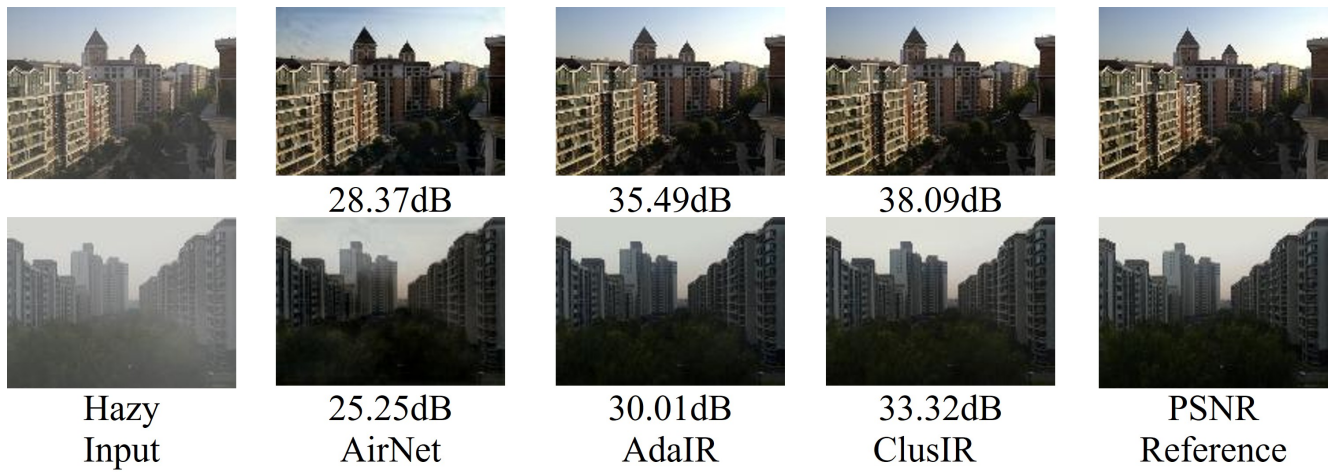


Figure 14. Dehazing visual comparisons of ClusIR with state-of-the-art All-in-One methods under One-by-One setting.

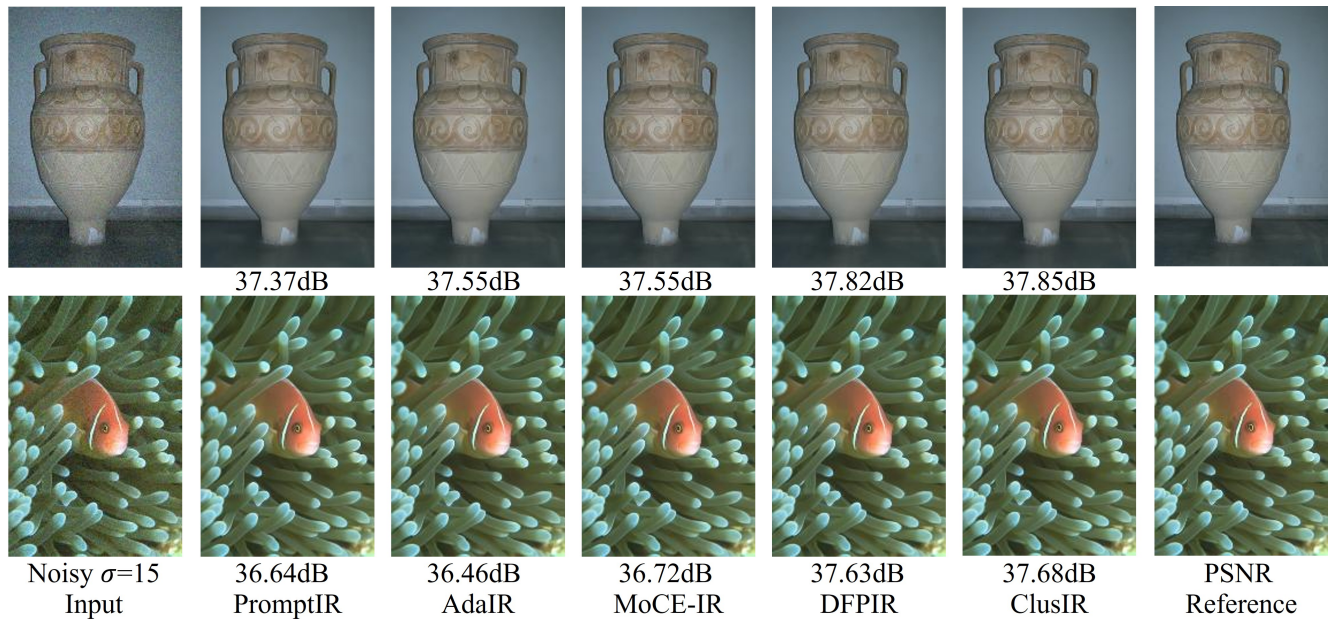


Figure 15. Denoising ( $\sigma = 15$ ) visual comparisons of ClusIR with state-of-the-art All-in-One methods under “N+H+R” setting.

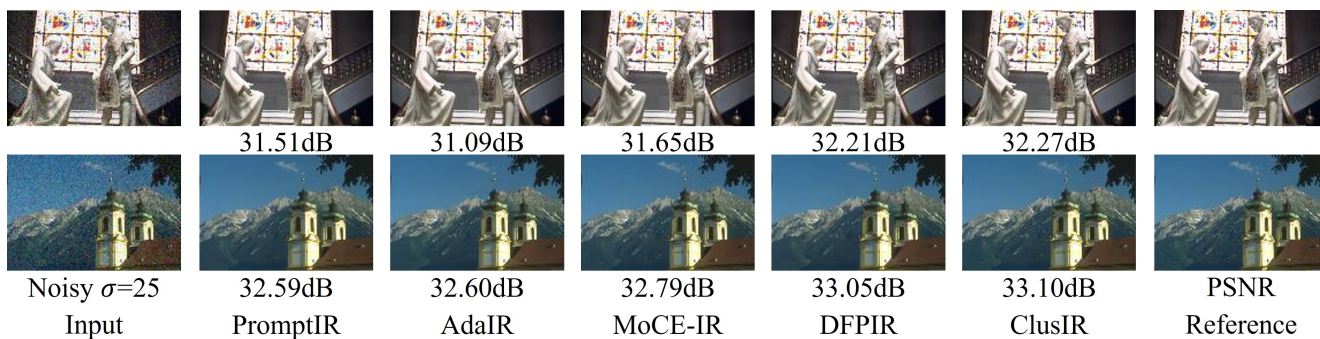


Figure 16. Denoising ( $\sigma = 25$ ) visual comparisons of ClusIR with state-of-the-art All-in-One methods under “N+H+R” setting.



Figure 17. Denoising ( $\sigma = 50$ ) visual comparisons of ClusIR with state-of-the-art All-in-One methods under “N+H+R” setting.

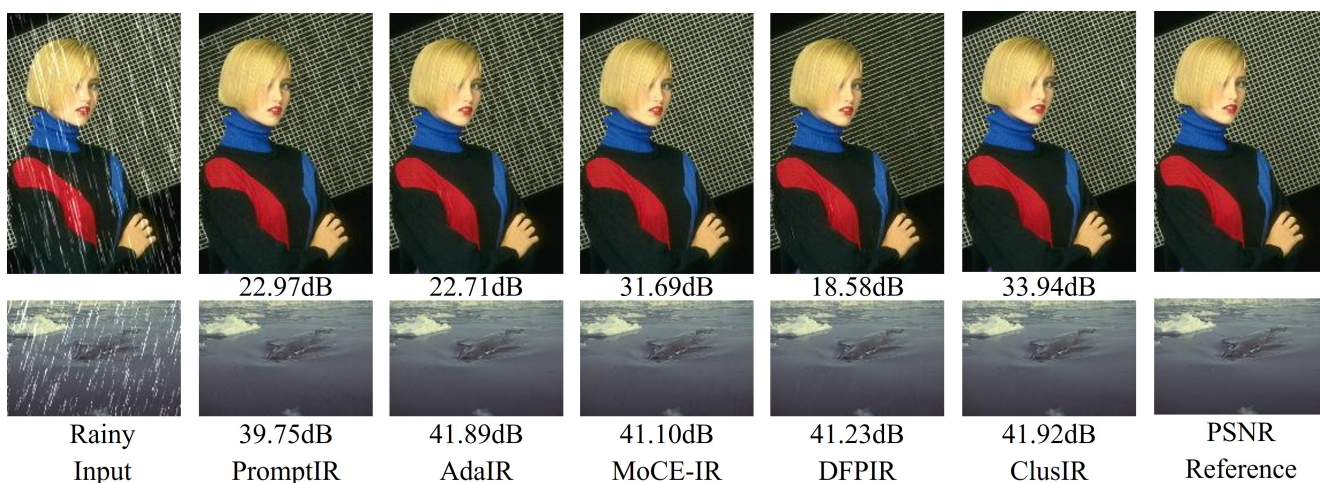


Figure 18. Deraining visual comparisons of ClusIR with state-of-the-art All-in-One methods under “N+H+R” setting.

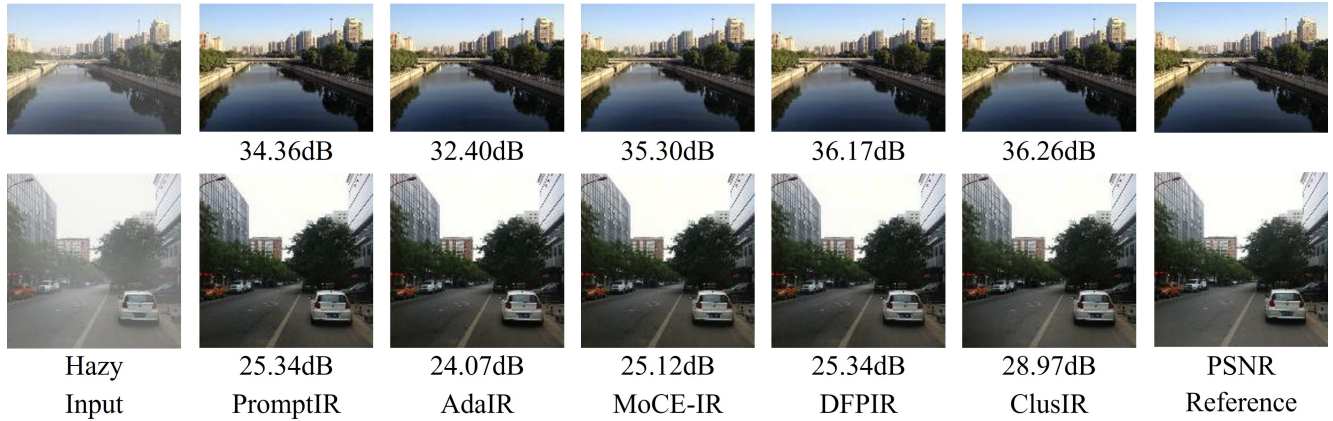


Figure 19. Dehazing visual comparisons of ClusIR with state-of-the-art All-in-One methods under “N+H+R” setting.

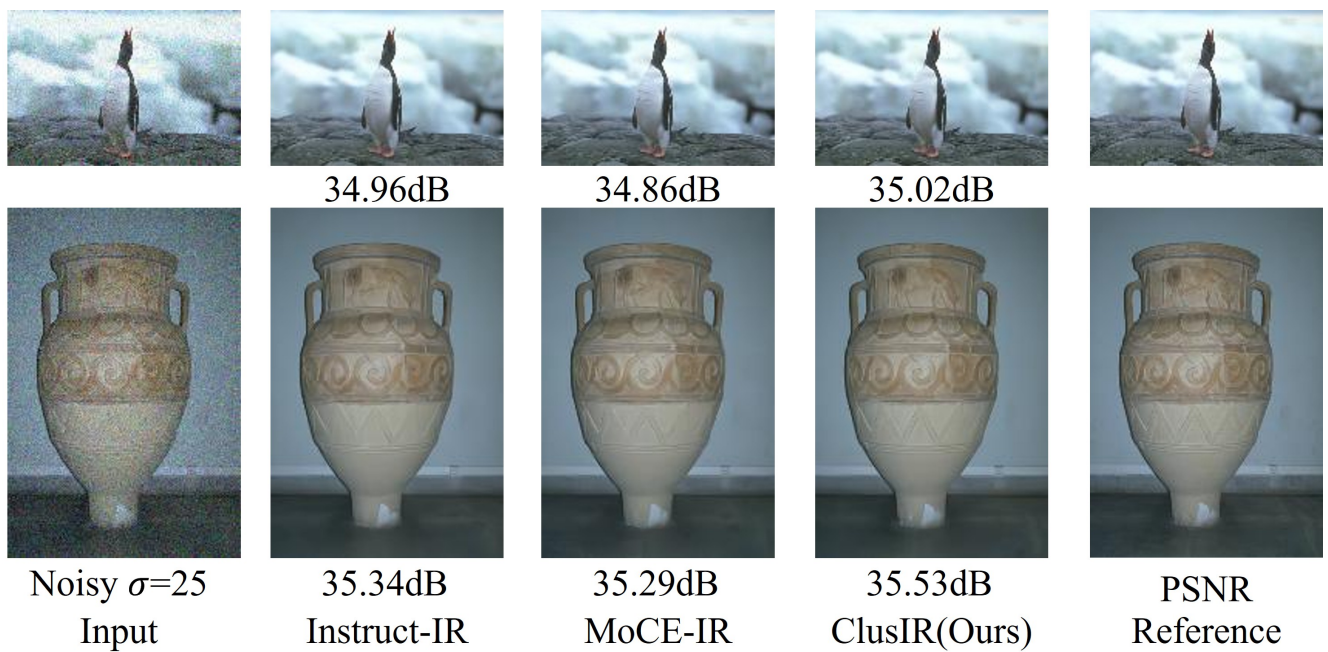


Figure 20. Denoising ( $\sigma = 25$ ) visual comparisons of ClusIR with state-of-the-art All-in-One methods under “N+H+R+B+L” setting.

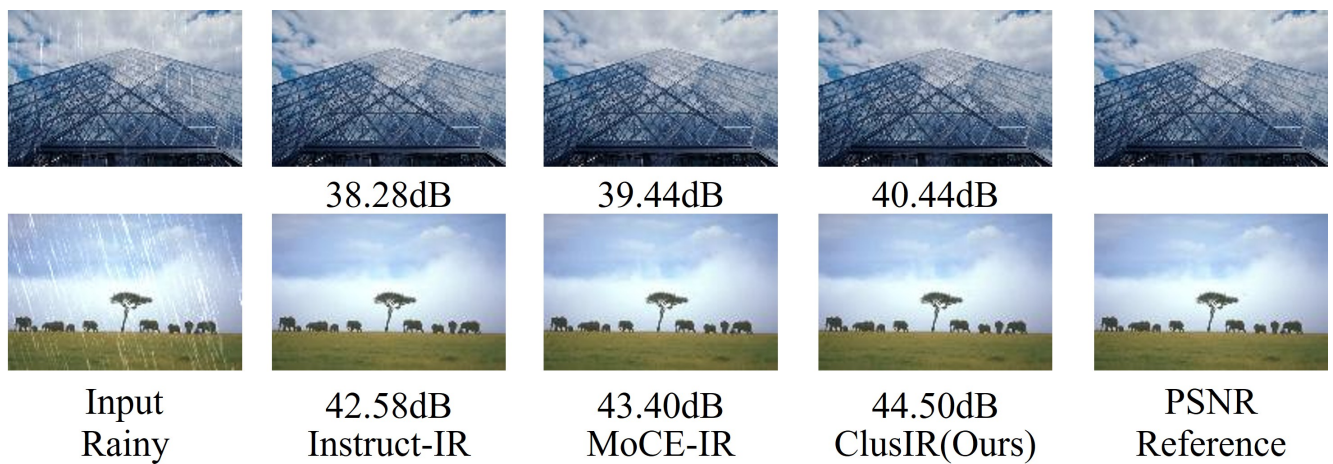


Figure 21. Deraining visual comparisons of ClusIR with state-of-the-art All-in-One methods under “N+H+R+B+L” setting.

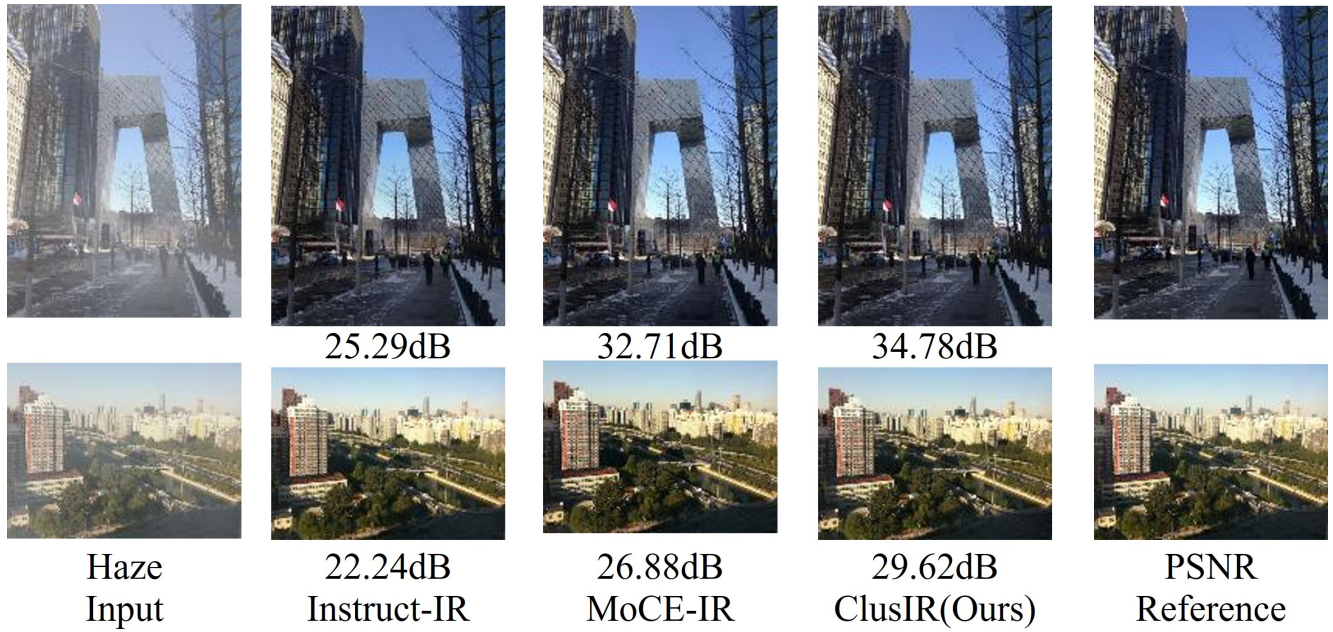


Figure 22. Dehazing visual comparisons of ClusIR with state-of-the-art All-in-One methods under “N+H+R+B+L” setting.

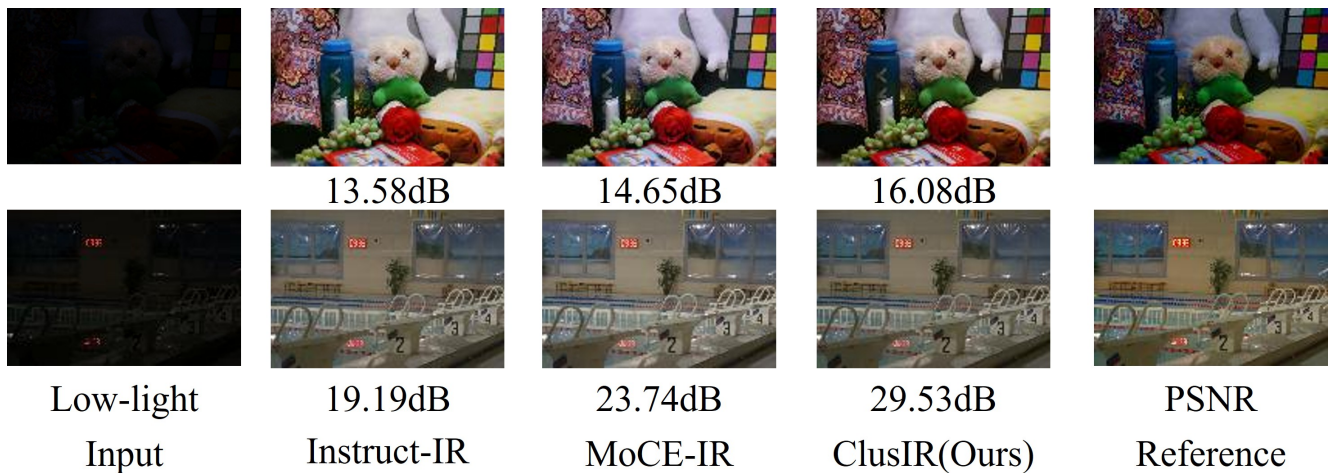


Figure 23. Enhancement visual comparisons of ClusIR with state-of-the-art All-in-One methods under “N+H+R+B+L” setting.

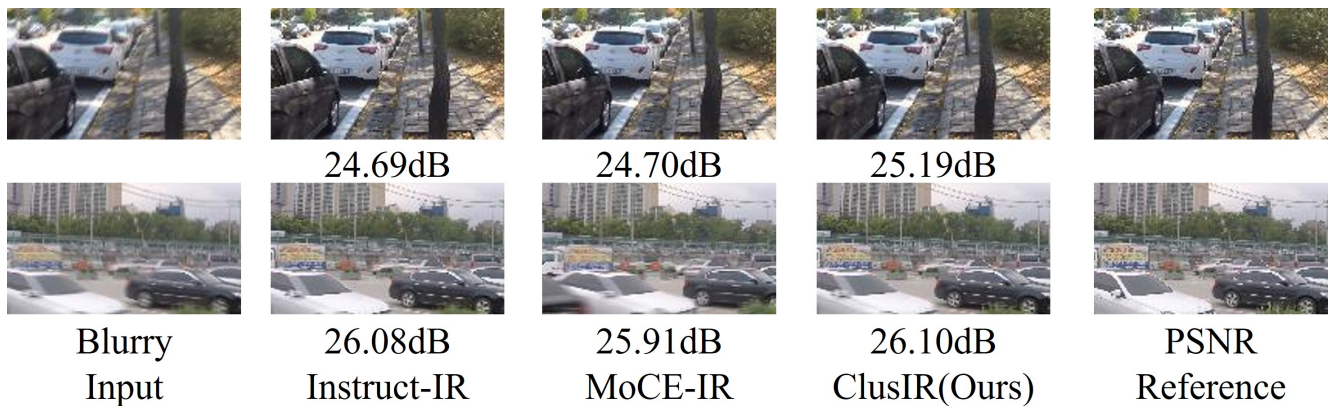


Figure 24. Deblurring visual comparisons of ClusIR with state-of-the-art All-in-One methods under “N+H+R+B+L” setting.

## References

- [1] Pablo Arbelaez, Michael Maire, Charless Fowlkes, and Jitendra Malik. Contour detection and hierarchical image segmentation. *IEEE Trans. Pattern Anal. Mach. Intell.*, 33(5): 898–916, 2010. 6, 10
- [2] Bolun Cai, Xiangmin Xu, Kui Jia, Chunmei Qing, and Dacheng Tao. Dehazenet: An end-to-end system for single image haze removal. *IEEE Trans. Image Process.*, 25(11): 5187–5198, 2016. 1, 2, 7
- [3] Yuanhao Cai, Hao Bian, Jing Lin, Haoqian Wang, Radu Timofte, and Yulun Zhang. Retinexformer: One-stage retinex-based transformer for low-light image enhancement. In *Proc. IEEE/CVF Int. Conf. Comput. Vis. (ICCV)*, pages 12504–12513, 2023. 1, 2, 7
- [4] Mathilde Caron, Hugo Touvron, Ishan Misra, Hervé Jégou, Julien Mairal, Piotr Bojanowski, and Armand Joulin. Emerging properties in self-supervised vision transformers. In *Proc. IEEE/CVF Int. Conf. Comput. Vis. (ICCV)*, pages 9650–9660, 2021. 2
- [5] Liangyu Chen, Xiaojie Chu, Xiangyu Zhang, and Jian Sun. Simple baselines for image restoration. In *Proc. Eur. Conf. Comput. Vis. (ECCV)*, pages 17–33, 2022. 1, 7
- [6] Xiang Chen, Hao Li, Mingqiang Li, and Jinshan Pan. Learning a sparse transformer network for effective image deraining. In *Proc. IEEE/CVF Conf. Comput. Vis. Pattern Recognit. (CVPR)*, pages 5896–5905, 2023. 7
- [7] Zheng Chen, Yulun Zhang, Ding Liu, Bin Xia, Jinjin Gu, Linghe Kong, and Xin Yuan. Hierarchical integration diffusion model for realistic image deblurring. In *Adv. Neural Inf. Process. Syst. (NeurIPS)*, pages 29114–29125, 2023. 7
- [8] Marcos V Conde, Gregor Geigle, and Radu Timofte. High-quality image restoration following human instructions. In *Proc. Eur. Conf. Comput. Vis. (ECCV)*, pages 1–21, 2024. 6, 12
- [9] Yuning Cui, Wenqi Ren, Xiaochun Cao, and Alois Knoll. Image restoration via frequency selection. *IEEE Trans. Pattern Anal. Mach. Intell.*, 46(2):1093–1108, 2023. 1, 7
- [10] Yuning Cui, Mingyu Liu, Wenqi Ren, and Alois Knoll. Hybrid frequency modulation network for image restoration. In *Proc. 33rd Int. Joint Conf. Artif. Intell.*, pages 722–730, 2024. 2
- [11] Yuning Cui, Syed Waqas Zamir, Salman H. Khan, Alois Knoll, Mubarak Shah, and Fahad Shahbaz Khan. Adair: Adaptive all-in-one image restoration via frequency mining and modulation. In *Int. Conf. Learn. Represent. (ICLR)*, 2025. 2, 6, 11
- [12] Yu Dong, Yihao Liu, He Zhang, Shifeng Chen, and Yu Qiao. FD-GAN: generative adversarial networks with fusion-discriminator for single image dehazing. In *Proc. AAAI Conf. Artif. Intell. (AAAI)*, pages 10729–10736, 2020. 1, 7
- [13] Rich Franzen. Kodak Lossless True Color Image Suite, 1999. [Online]. Available: <http://r0k.us/graphics/kodak/> [Accessed: Oct. 24, 2021]. 6
- [14] Hongyun Gao, Xin Tao, Xiaoyong Shen, and Jiaya Jia. Dynamic scene deblurring with parameter selective sharing and nested skip connections. In *Proc. IEEE/CVF Conf. Comput. Vis. Pattern Recognit. (CVPR)*, pages 3848–3856, 2019. 7
- [15] Yu Guo, Yuan Gao, Yuxu Lu, Huilin Zhu, Ryan Wen Liu, and Shengfeng He. Onerestore: A universal restoration framework for composite degradation. In *Proc. Eur. Conf. Comput. Vis. (ECCV)*, pages 255–272. Springer, 2024. 6, 10
- [16] Shengkai Hu, Haozhe Qi, Jun Wan, Jiaying Huang, Lefei Zhang, Hang Sun, and Dacheng Tao. Proto-former: Unified facial landmark detection by prototype transformer. *arXiv preprint arXiv:2510.15338*, 2025. 1
- [17] Jia-Bin Huang, Abhishek Singh, and Narendra Ahuja. Single image super-resolution from transformed self-exemplars. In *Proc. IEEE/CVF Conf. Comput. Vis. Pattern Recognit. (CVPR)*, pages 5197–5206, 2015. 10
- [18] Xin Huang, Ding Wang, Qiqi Zhu, Ying Zheng, and Qingfeng Guan. Single target tracking in high-resolution satellite videos: a comprehensive review. *Geo-Spatial Information Science*, 28(3):966–995, 2025. 1
- [19] Jiachen Jiang, Tianyu Ding, Ke Zhang, Jinxin Zhou, Tianyi Chen, Ilya Zharkov, Zhihui Zhu, and Luming Liang. Cat-air: Content and task-aware all-in-one image restoration. *arXiv preprint arXiv:2503.17915*, 2025. 2
- [20] Orest Kupyn, Volodymyr Budzan, Mykola Mykhailych, Dmytro Mishkin, and Jiří Matas. Deblurgan: Blind motion deblurring using conditional adversarial networks. In *Proc. IEEE/CVF Conf. Comput. Vis. Pattern Recognit. (CVPR)*, pages 8183–8192, 2018. 7
- [21] Boyi Li, Wenqi Ren, Dengpan Fu, Dacheng Tao, Dan Feng, Wenjun Zeng, and Zhangyang Wang. Benchmarking single-image dehazing and beyond. *IEEE Trans. Image Process.*, 28(1):492–505, 2018. 6, 10
- [22] Boyun Li, Xiao Liu, Peng Hu, Zhongqin Wu, Jiancheng Lv, and Xi Peng. All-in-one image restoration for unknown corruption. In *Proc. IEEE/CVF Conf. Comput. Vis. Pattern Recognit. (CVPR)*, pages 17452–17462, 2022. 2, 6, 7, 10, 11
- [23] Bingchen Li, Xin Li, Yiting Lu, and Zhibo Chen. Hybrid agents for image restoration. *arXiv preprint arXiv:2503.10120*, 2025. 2
- [24] Ziyang Lihe, Qiangqiang Yuan, Jiang He, Xianyu Jin, Yi Xiao, Yuzeng Chen, Huanfeng Shen, and Liangpei Zhang. Ada4dir: An adaptive model-driven all-in-one image restoration network for remote sensing images. *Information Fusion*, 118:102930, 2025. 2
- [25] Jingbo Lin, Zhilu Zhang, Wenbo Li, Renjing Pei, Hang Xu, Hongzhi Zhang, and Wangmeng Zuo. Unirestorer: Universal image restoration via adaptively estimating image degradation at proper granularity. *arXiv preprint arXiv:2412.20157*, 2024. 2, 3
- [26] Xin Lin, Jingtong Yue, Kelvin CK Chan, Lu Qi, Chao Ren, Jinshan Pan, and Ming-Hsuan Yang. Multi-task image restoration guided by robust dino features. *arXiv preprint arXiv:2312.01677*, 2023. 2
- [27] Lin Liu, Lingxi Xie, Xiaopeng Zhang, Shanxin Yuan, Xiangyu Chen, Wengang Zhou, Houqiang Li, and Qi Tian. Tape: Task-agnostic prior embedding for image restoration. In *Proc. Eur. Conf. Comput. Vis. (ECCV)*, pages 447–464, 2022. 6

- [28] Minghao Liu, Wenhan Yang, Jinyi Luo, and Jiaying Liu. Up-restorer: When unrolling meets prompts for unified image restoration. In *Proc. AAAI Conf. Artif. Intell. (AAAI)*, pages 5513–5522, 2025. 6
- [29] Tong Liu, Jing Li, Jia Wu, Bo Du, Yibing Zhan, Dapeng Tao, and Jun Wan. Facial expression recognition with heatmap neighbor contrastive learning. *IEEE Trans. Multimedia*, 2025. 1
- [30] Yulin Luo, Rui Zhao, Xiaobao Wei, Jinwei Chen, Yijie Lu, Shenghao Xie, Tianyu Wang, Ruiqin Xiong, Ming Lu, and Shanghang Zhang. Wm-moe: Weather-aware multi-scale mixture-of-experts for blind adverse weather removal. *arXiv preprint arXiv:2303.13739*, 2023. 2
- [31] Jiaqi Ma, Tianheng Cheng, Guoli Wang, Qian Zhang, Xinggang Wang, and Lefei Zhang. Prores: Exploring degradation-aware visual prompt for universal image restoration. *arXiv preprint arXiv:2306.13653*, 2023. 2, 6
- [32] Kede Ma, Zhengfang Duanmu, Qingbo Wu, Zhou Wang, Hongwei Yong, Hongliang Li, and Lei Zhang. Waterloo exploration database: New challenges for image quality assessment models. *IEEE Trans. Image Process.*, 26(2):1004–1016, 2016. 6, 10
- [33] David Martin, Charless Fowlkes, Doron Tal, and Jitendra Malik. A database of human segmented natural images and its application to evaluating segmentation algorithms and measuring ecological statistics. In *Proc. IEEE/CVF Int. Conf. Comput. Vis. (ICCV)*, pages 416–423, 2001. 6, 10
- [34] Seungjun Nah, Tae Hyun Kim, and Kyoung Mu Lee. Deep multi-scale convolutional neural network for dynamic scene deblurring. In *Proc. IEEE/CVF Conf. Comput. Vis. Pattern Recognit. (CVPR)*, pages 3883–3891, 2017. 6, 10
- [35] Jim Nilsson and Tomas Akenine-Möller. Understanding ssim. *arXiv preprint arXiv:2006.13846*, 2020. 6
- [36] Maxime Oquab, Timothée Darcet, Théo Moutakanni, Huy Vo, Marc Szafraniec, Vasil Khalidov, Pierre Fernandez, Daniel Haziza, Francisco Massa, Alaaeldin El-Nouby, et al. Dinov2: Learning robust visual features without supervision. *arXiv preprint arXiv:2304.07193*, 2023. 2
- [37] Ozan Özdenizci and Robert Legenstein. Restoring vision in adverse weather conditions with patch-based denoising diffusion models. *IEEE Trans. Pattern Anal. Mach. Intell.*, 45(8):10346–10357, 2023. 10, 11
- [38] Vaishnav Potlapalli, Syed Waqas Zamir, Salman Khan, and Fahad Shahbaz Khan. Promptir: Prompting for all-in-one blind image restoration. In *Adv. Neural Inf. Process. Syst. (NeurIPS)*, pages 71275–71293, 2023. 2, 3, 6, 7, 10, 11
- [39] Alec Radford, Jong Wook Kim, Chris Hallacy, Aditya Ramesh, Gabriel Goh, Sandhini Agarwal, Girish Sastry, Amanda Askell, Pamela Mishkin, Jack Clark, et al. Learning transferable visual models from natural language supervision. In *Proc. Int. Conf. Mach. Learn. (ICML)*, pages 8748–8763. PmLR, 2021. 2
- [40] Hao Shen, Zhong-Qiu Zhao, and Wandu Zhang. Adaptive dynamic filtering network for image denoising. In *Proc. AAAI Conf. Artif. Intell. (AAAI)*, pages 2227–2235, 2023. 1, 7
- [41] Yuda Song, Zhuqing He, Hui Qian, and Xin Du. Vision transformers for single image dehazing. *IEEE Trans. Image Process.*, 32:1927–1941, 2023. 1, 7
- [42] Xiaole Tang, Xiaoyi He, Xiang Gu, and Jian Sun. Baryir: Learning multi-source unified representation in continuous barycenter space for generalizable all-in-one image restoration. *arXiv preprint arXiv:2505.21637*, 2025. 2
- [43] Xiangpeng Tian, Xiangyu Liao, Xiao Liu, Meng Li, and Chao Ren. Degradation-aware feature perturbation for all-in-one image restoration. In *Proc. IEEE/CVF Conf. Comput. Vis. Pattern Recognit. (CVPR)*, pages 28165–28175, 2025. 6, 11
- [44] Fu-Jen Tsai, Yan-Tsung Peng, Yen-Yu Lin, Chung-Chi Tsai, and Chia-Wen Lin. Stripformer: Strip transformer for fast image deblurring. In *Proc. Eur. Conf. Comput. Vis. (ECCV)*, pages 146–162, 2022. 7
- [45] Jeya Maria Jose Valanarasu, Rajeev Yasarla, and Vishal M Patel. Transweather: Transformer-based restoration of images degraded by adverse weather conditions. In *Proc. IEEE/CVF Conf. Comput. Vis. Pattern Recognit. (CVPR)*, pages 2353–2363, 2022. 6
- [46] Jun Wan, Jun Liu, Jie Zhou, Zhihui Lai, Linlin Shen, Hang Sun, Ping Xiong, and Wenwen Min. Precise facial landmark detection by reference heatmap transformer. *IEEE Trans. Image Process.*, 32:1966–1977, 2023. 1
- [47] Sirui Wang, Jiang He, Natalia Blasco Andreo, and Xiao Xiang Zhu. Gewdiff: Geometric enhanced wavelet-based diffusion model for hyperspectral image super-resolution. *arXiv preprint arXiv:2511.07103*, 2025. 2
- [48] Tao Wang, Kaihao Zhang, Ziqian Shao, Wenhan Luo, Bjorn Stenger, Tong Lu, Tae-Kyun Kim, Wei Liu, and Hongdong Li. Gridformer: Residual dense transformer with grid structure for image restoration in adverse weather conditions. *Int. J. Comput. Vis.*, 132(10):4541–4563, 2024. 6
- [49] Yongzhen Wang, Yongjun Li, Zhuoran Zheng, Xiao-Ping Zhang, and Mingqiang Wei. M2restore: Mixture-of-experts-based mamba-cnn fusion framework for all-in-one image restoration. *arXiv preprint arXiv:2506.07814*, 2025. 2, 3
- [50] Chen Wei, Wenjing Wang, Wenhan Yang, and Jiaying Liu. Deep retinex decomposition for low-light enhancement. In *Proc. Brit. Mach. Vis. Conf. (BMVC)*, 2018. 6, 10
- [51] Gang Wu, Junjun Jiang, Kui Jiang, Xianming Liu, and Liqiang Nie. Dswinir: Rethinking window-based attention for image restoration, 2025. 2
- [52] Wenhui Wu, Jian Weng, Pingping Zhang, Xu Wang, Wenhan Yang, and Jianmin Jiang. Uretinex-net: Retinex-based deep unfolding network for low-light image enhancement. In *Proc. IEEE/CVF Conf. Comput. Vis. Pattern Recognit. (CVPR)*, pages 5901–5910, 2022. 1, 2, 7
- [53] Bin Xia, Yulun Zhang, Shiyin Wang, Yitong Wang, Xinglong Wu, Yapeng Tian, Wenming Yang, and Luc Van Gool. Diffir: Efficient diffusion model for image restoration. In *Proc. IEEE/CVF Int. Conf. Comput. Vis. (ICCV)*, pages 13095–13105, 2023. 7
- [54] Zeyu Xiao, Zhuoyuan Li, and Wei Jia. Occlusion-embedded hybrid transformer for light field super-resolution. In *AAAI Conf. Artif. Intell. (AAAI)*, pages 8700–8708, 2025. 1
- [55] Xiaogang Xu, Ruixing Wang, and Jiangbo Lu. Low-light image enhancement via structure modeling and guidance. In *Proc. IEEE/CVF Conf. Comput. Vis. Pattern Recognit. (CVPR)*, pages 9893–9903, 2023. 7

- [56] Hao Yang, Liyuan Pan, Yan Yang, and Wei Liang. Language-driven all-in-one adverse weather removal. In *Proc. IEEE/CVF Conf. Comput. Vis. Pattern Recognit. (CVPR)*, pages 24902–24912, 2024. 2
- [57] Wenhan Yang, Robby T Tan, Jiashi Feng, Jiaying Liu, Zongming Guo, and Shuicheng Yan. Deep joint rain detection and removal from a single image. In *Proc. IEEE/CVF Conf. Comput. Vis. Pattern Recognit. (CVPR)*, pages 1357–1366, 2017. 6, 10
- [58] Mingde Yao, Ruikang Xu, Yuanshen Guan, Jie Huang, and Zhiwei Xiong. Neural degradation representation learning for all-in-one image restoration. *IEEE Trans. Image Process.*, 33:5408–5423, 2024. 6
- [59] Ting Yao, Yingwei Pan, Yehao Li, Chong-Wah Ngo, and Tao Mei. Wave-vit: Unifying wavelet and transformers for visual representation learning. In *Proc. Eur. Conf. Comput. Vis. (ECCV)*, pages 328–345. Springer, 2022. 3
- [60] Rajeev Yasarla and Vishal M Patel. Uncertainty guided multi-scale residual learning-using a cycle spinning cnn for single image de-raining. In *Proc. IEEE/CVF Conf. Comput. Vis. Pattern Recognit. (CVPR)*, pages 8405–8414, 2019. 7
- [61] Xiaoyan Yu, Shen Zhou, Huafeng Li, and Liehuang Zhu. Multi-expert adaptive selection: Task-balancing for all-in-one image restoration. *IEEE Trans. Circuits Syst. Video Technol.*, 2024. 2, 3
- [62] Eduard Zamfir, Zongwei Wu, Nancy Mehta, Yuedong Tan, Danda Pani Paudel, Yulun Zhang, and Radu Timofte. Complexity experts are task-discriminative learners for any image restoration. In *Proc. IEEE/CVF Conf. Comput. Vis. Pattern Recognit. (CVPR)*, pages 12753–12763, 2025. 2, 6, 11, 12
- [63] Syed Waqas Zamir, Aditya Arora, Salman Khan, Munawar Hayat, Fahad Shahbaz Khan, Ming-Hsuan Yang, and Ling Shao. Learning enriched features for real image restoration and enhancement. In *Proc. Eur. Conf. Comput. Vis. (ECCV)*, pages 492–511, 2020. 1, 7
- [64] Syed Waqas Zamir, Aditya Arora, Salman H. Khan, Munawar Hayat, Fahad Shahbaz Khan, Ming-Hsuan Yang, and Ling Shao. Multi-stage progressive image restoration. In *Proc. IEEE/CVF Conf. Comput. Vis. Pattern Recognit. (CVPR)*, pages 14816–14826, 2021. 2, 7
- [65] Syed Waqas Zamir, Aditya Arora, Salman Khan, Munawar Hayat, Fahad Shahbaz Khan, and Ming-Hsuan Yang. Restormer: Efficient transformer for high-resolution image restoration. In *Proc. IEEE/CVF Conf. Comput. Vis. Pattern Recognit. (CVPR)*, pages 5728–5739, 2022. 1, 7
- [66] Syed Waqas Zamir, Aditya Arora, Salman Khan, Munawar Hayat, Fahad Shahbaz Khan, Ming-Hsuan Yang, and Ling Shao. Learning enriched features for fast image restoration and enhancement. *IEEE Trans. Pattern Anal. Mach. Intell.*, 45(2):1934–1948, 2022. 1, 2, 7
- [67] Jinghao Zhang, Jie Huang, Mingde Yao, Zizheng Yang, Hu Yu, Man Zhou, and Feng Zhao. Ingredient-oriented multi-degradation learning for image restoration. In *Proc. IEEE/CVF Conf. Comput. Vis. Pattern Recognit. (CVPR)*, pages 5825–5835, 2023. 6, 7
- [68] Junyi Zhang, Charles Herrmann, Junhwa Hur, Luisa Polania Cabrera, Varun Jampani, Deqing Sun, and Ming-Hsuan Yang. A tale of two features: Stable diffusion complements dino for zero-shot semantic correspondence. In *Adv. Neural Inf. Process. Syst. (NeurIPS)*, 2024. 2
- [69] Kai Zhang, Wangmeng Zuo, Yunjin Chen, Deyu Meng, and Lei Zhang. Beyond a gaussian denoiser: Residual learning of deep cnn for image denoising. *IEEE Trans. Image Process.*, 26(7):3142–3155, 2017. 1, 7
- [70] Kai Zhang, Wangmeng Zuo, and Lei Zhang. Ffdnet: Toward a fast and flexible solution for cnn-based image denoising. *IEEE Trans. Image Process.*, 27(9):4608–4622, 2018. 1, 7
- [71] Rongyu Zhang, Yulin Luo, Jiaming Liu, Huanrui Yang, Zhen Dong, Denis Gudovskiy, Tomoyuki Okuno, Yohei Nakata, Kurt Keutzer, Yuan Du, et al. Efficient deweahter mixture-of-experts with uncertainty-aware feature-wise linear modulation. In *AAAI Conf. Artif. Intell. (AAAI)*, pages 16812–16820, 2024. 2
- [72] Xu Zhang, Jiaqi Ma, Guoli Wang, Qian Zhang, Huan Zhang, and Lefei Zhang. Perceive-ir: Learning to perceive degradation better for all-in-one image restoration. *IEEE Trans. Image Process.*, pages 1–1, 2025. 2, 6, 7
- [73] Shihao Zhou, Jinshan Pan, Jinglei Shi, Duosheng Chen, Lishen Qu, and Jufeng Yang. Seeing the unseen: A frequency prompt guided transformer for image restoration. In *Proc. Eur. Conf. Comput. Vis. (ECCV)*, pages 246–264. Springer, 2024. 2
- [74] Yurui Zhu, Tianyu Wang, Xueyang Fu, Xuanyu Yang, Xin Guo, Jifeng Dai, Yu Qiao, and Xiaowei Hu. Learning weather-general and weather-specific features for image restoration under multiple adverse weather conditions. In *Proc. IEEE/CVF Conf. Comput. Vis. Pattern Recognit. (CVPR)*, pages 21747–21758, 2023. 10, 11